

## Review Article

# Graphene and g-C<sub>3</sub>N<sub>4</sub>-Based Gas Sensors

**Ahmed Kotbi,<sup>1,2</sup> Mohammed Imran,<sup>3</sup> Khaled Kaja,<sup>4</sup> Ariful Rahaman,<sup>3</sup> El Mostafa Ressami,<sup>2</sup> Michael Lejeune,<sup>1</sup> Brahim Lakssir,<sup>2</sup> and Mustapha Jouiad<sup>1</sup>** 

<sup>1</sup>Laboratory of Physics of Condensed Matter, University of Picardie Jules Verne, Amiens 80039, France

<sup>2</sup>Moroccan Foundation for Advanced Science, Innovation and Research, Madinat Al Irfane, Rabat 10100, Morocco

<sup>3</sup>School of Mechanical Engineering, Vellore Institute of Technology, Vellore, Tamil Nadu 632014, India

<sup>4</sup>Laboratoire National de Métrologie et D'essais (LNE), 29 Av. Roger Hannequin, Trappes 78197, France

Correspondence should be addressed to Mustapha Jouiad; [mustapha.jouiad@u-picardie.fr](mailto:mustapha.jouiad@u-picardie.fr)

Received 31 October 2021; Accepted 29 January 2022; Published 27 February 2022

Academic Editor: Eduard Llobet

Copyright © 2022 Ahmed Kotbi et al. This is an open access article distributed under the Creative Commons Attribution License, which permits unrestricted use, distribution, and reproduction in any medium, provided the original work is properly cited.

The efficient monitoring of the environment is currently gaining a continuous growing interest in view of finding solutions for the global pollution issues and their associated climate change. In this sense, two-dimensional (2D) materials appear as one of highly attractive routes for the development of efficient sensing devices due, in particular, to the interesting blend of their superlative properties. For instance, graphene (Gr) and graphitic carbon nitride g-C<sub>3</sub>N<sub>4</sub> (g-CN) have specifically attracted great attention in several domains of sensing applications owing to their excellent electronic and physical-chemical properties. Despite the high potential they offer in the development and fabrication of high-performance gas-sensing devices, an exhaustive comparison between Gr and g-CN is not well established yet regarding their electronic properties and their sensing performances such as sensitivity and selectivity. Hence, this work aims at providing a state-of-the-art overview of the latest experimental advances in the fabrication, characterization, development, and implementation of these 2D materials in gas-sensing applications. Then, the reported results are compared to our numerical simulations using density functional theory carried out on the interactions of Gr and g-CN with some selected hazardous gases' molecules such as NO<sub>2</sub>, CO<sub>2</sub>, and HF. Our findings conform with the superior performances of the g-CN regarding HF detection, while both g-CN and Gr show comparable detection performances for the remaining considered gases. This allows suggesting an outlook regarding the future use of these 2D materials as high-performance gas sensors.

## 1. Introduction

A fast-paced race for devices' miniaturization based on 2D materials is marking the particularly rapid evolution in the research and development of carbon nanomaterials (CNM) in biomedical systems, electronic appliances, computing devices, and sensor manufacturing industries [1–5]. Advancements in these application fields depend on the ability to grow CNM on various substrates, with controlled morphologies and quality, while increasing their efficiency of getting assembled in complex architectures [6]. Since its first isolation in 2004, graphene (Gr) has constantly been the highlight superlative star of 2D materials. Formed by sp<sup>2</sup>-hybridized carbon atoms bonded covalently and packed densely to form honeycomb crystal lattice [7, 8], graphene is

a single-atom-thick sheet semimetal with commendable electron transport properties and superior thermal and electrical conductivities in addition to superior mechanical properties [9–13]. In contrast to graphene, graphitic carbon nitride g-C<sub>3</sub>N<sub>4</sub> (g-CN) is a semiconducting nanomaterial with a crystal structure analogous to graphite constructed from Van der Waals sheets of sp<sup>2</sup> hybrid carbon and nitrogen atoms. g-CN is an abundant, inexpensive, and easy to manufacture nanomaterial at large scale [14]. This, added to its high electrical properties and good thermal and chemical stabilities, has recently created an increasing interest around it. With an appropriate bandgap and high electron mobility, g-CN also constitutes a potentially good candidate for various applications in energy storage, solar cells, gas sensing, and catalysis [15–18].

Gas sensing is one of the important applications of Gr and associated 2D nanomaterials, owing mainly to several interesting properties such as (i) large surface area (for Gr  $2630 \text{ m}^2/\text{g}$ ), (ii) good conductivity, (iii) high gas sensitivity, (iv) and the possibility of tailored surface functionalization for a specific gas absorption. In Gr, the gas absorption is a result of a pull electron effect [19, 20]. In fact, the adsorbed molecules change the Fermi level of Gr and hence its conductivity, due to hybridization and coupling on its surface. They act as electron donors in case their valence band energy is higher than the Fermi level of Gr and as electron acceptors in the opposite case when the valence band energy is lower than Fermi level of Gr [21, 22].

Nowadays, highly performing portable sensors have become a key necessity for all technological advances. While metal-oxide-semiconductor based gas sensors are far commonly used, their performances remain very limited due to their short life, poor selectivity, temperature instabilities, and high sensitivity to environment's perturbations. The use of nanostructured materials with higher gas-sensing capabilities has therefore become inevitable [5].

Besides, the development of g-CN based gas sensors, compared to those based on Gr or transition metal disulfide nanosheets, is becoming more attractive [23]. Many approaches have been adopted so far for the development of this material in view of its incorporation in gas-sensing applications. In this sense, researchers attempted to combine g-CN with other materials to improve its performances [24]. For instance, the use of porous g-CN in nanostructure designs as gas sensors appeared to greatly improve their selectivity and their sensitivity in ambient conditions. Similarly, hybridization of g-CN with other materials was found as a promising route for further enhancement in detection performances [23]. The resulting heterostructures made of metal oxide nanoparticles attached to the surface of 2D materials were found to exhibit higher detection properties [14]. For instance, g-CN/ $\text{MO}_x$  heterostructures revealed much superior detection performances compared to a pure  $\text{MO}_x$  sensor ( $\text{MnO}_2$ ,  $\text{ZnO}$ , and  $\text{TiO}_2$ ). However, some drawbacks remain, which prevent the direct application of these sensors, such as the high working temperature and the slow sensing response [25]. These achievements are attributed, on one hand, to the increased surface area obtained by the combination of 2D g-CN with the  $\text{MO}_x$  leading to an increased number of gas-material interaction sites [20] and to the low operating temperature while improving the gas sensitivity and selectivity on the other hand [23]. Despite these interesting gas-sensing performances, g-CN presents some limitations when compared to Gr such as its moderate band gap that requires a high excitation voltage and its fast electron-hole pairs recombination leading to low responsivity. In addition, g-CN adsorbs most of gases and liquids, while Gr is known to be impermeable to most of fluids which reduces the operating temperature of graphene compared to g-CN.

In the following, we intend to provide a detailed overview of both CNM in terms of fabrication and characterization with special emphasis on their gas-sensing performances. Then theoretical calculations using density

functional theory (DFT) will be carried out to determine the adsorption mechanisms of selected gas molecules, namely,  $\text{CO}_2$ ,  $\text{NO}_2$ , and HF, and to examine the g-CN sensing performances to be compared to other graphitic nanomaterials such as Gr or reduced graphene oxide (r-GrO).

## 2. Synthesis of Graphene

Several methods are most commonly used for the fabrication of Gr layers including (i) micromechanical exfoliation, (ii) reduction of graphene oxide, (iii) chemical vapor deposition (CVD) [5, 26] or plasma-enhanced chemical vapor deposition (PECVD), and (iv) epitaxial growth on insulating materials. The choice of a fabrication route is mainly dependent upon the material quality and overall production cost required for given application.

The structural and vibrational properties of Gr are usually examined by Fourier-transform infrared spectroscopy (FTIR), X-ray diffraction (XRD), and Raman spectroscopy, respectively, and given in Figure 1 [27].

Transmission spectra (Figure 1(a)) show an obvious similarity for all three materials, mainly due to the C-C bond peaks present in the  $3225\text{--}1981 \text{ cm}^{-1}$  range. The XRD diagram (Figure 1(b)) shows a narrow diffraction peak at  $26.5^\circ$  ( $2\theta$ ) corresponding to the characteristic (002) plane of graphite. This peak is broadened and downshifted in graphene towards  $23.9^\circ$  representing an increased spacing of C-C layer in  $\text{sp}^2$  bonding. The Raman spectra (Figure 1(c)) show a characteristic vibration peak at  $1601 \text{ cm}^{-1}$  (G-band) related to the original graphitic structure for all three materials. However, a wider peak at  $1352 \text{ cm}^{-1}$  (D-band) appears for graphite oxide and Gr sheets related to the presence of defects in these structures. The ratio of these bands' intensities ( $I_D/I_G$ ) is a good indicator of the graphitization's quality in these layers.

**2.1. Mechanical Exfoliation.** Mechanical exfoliation is the first process through which Gr was isolated by Novoselov et al. [28]. It is a top-down approach in which Gr layers are exfoliated from bulk graphite using adhesive tape. The procedure involves repeated peeling of Gr from flakes of graphite. The tape containing Gr is finally placed on an Si/ $\text{SiO}_2$  surface and gently pressed to get Gr attached to the Si substrate. This method allows investigating the basic properties of Gr. For in-depth investigations of Gr properties for technical applications, scalable methods are being developed [29].

**2.2. Chemical Vapor Deposition.** Chemical vapor deposition (CVD) is the most common method used to produce Gr on a substrate with commendable quality and tailored dimensions. Growth mechanism and number of layers grown on the substrate depend on the catalyst metal substrate used such as Cu [26], Ni [30, 31], Cu-Ni alloy [1], and Co. Figure 2 shows a schematic of CVD setup used to grow carbon nanomaterials.

For Gr grown on Ni substrate, the Ni foil is annealed in hydrogen atmosphere and then carbon source gas such as

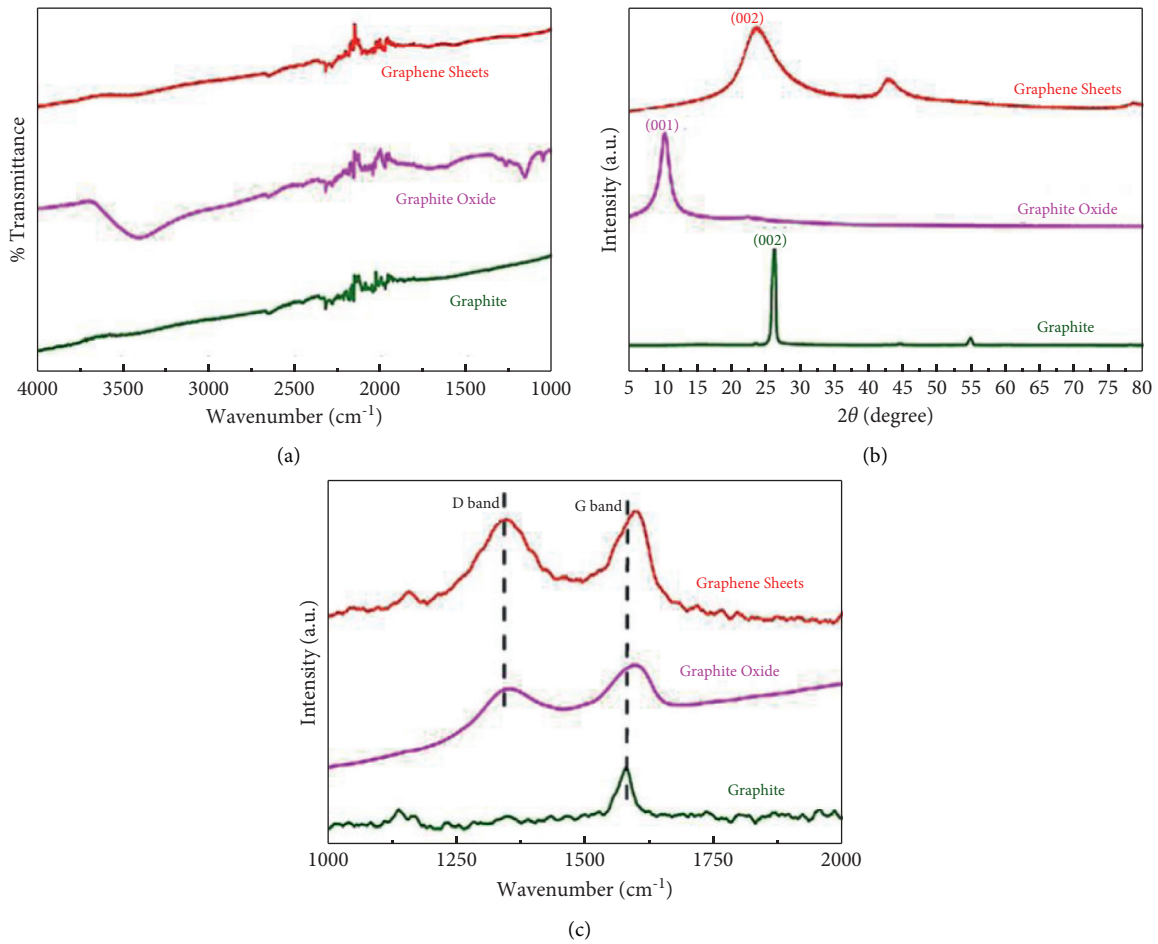


FIGURE 1: (a) FTIR, (b) XRD, and (c) Raman spectroscopy of graphite, graphite oxide, and graphene [27].

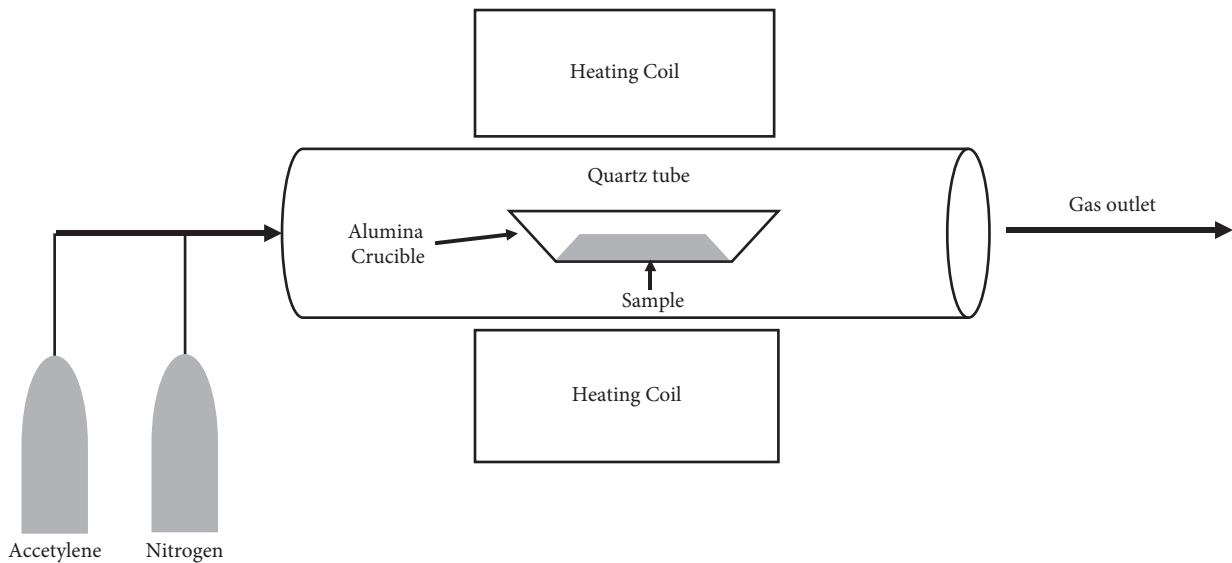


FIGURE 2: Schematic of CVD setup for graphene preparation [32].

methane or acetylene is admitted into the chamber. Argon gas is used during the process to maintain an inert atmosphere. A controlled cooling rate is necessary to produce

desired thicknesses of the Gr layers. Faster cooling rates yield thick graphite and slower cooling rates avoid segregation of carbon deposited on Ni foil [33]. If Ni foil grain growth is

small (few minutes of preannealing time) and chamber pressure is maintained high during growth step, nanosized graphite films are formed [30, 34] rather than few-layer Gr [5, 35]. Processing Gr on Cu substrate is most usually used to produce large-scale monolayer Gr films. The Cu foil is heated up to 1000°C in the presence of hydrogen atmosphere at low pressure and then carbon-containing gases such as methane or acetylene are admitted into the CVD chamber for 20–30 minutes and then gradually cooled. Table 1 shows comparison of Gr obtained using several fabrication methods [35].

Table 1 shows comparison of various properties of Gr synthesized through various methods. Gr synthesized through CVD shows a good mobility compared to Gr fabricated by other methods. Processing costs are also reduced with high volume of production by CVD technique.

Moreover, plasma-enhanced chemical vapor deposition (PECVD) was used as a potentially industrially scalable route for Gr synthesis. Kaindl et al. [42] have synthesized Gr on Si (100), Si/SiO<sub>2</sub>, Ni, Cu, MgO (100), and NaCl and on standard glass substrates using a mixture of C<sub>2</sub>H<sub>2</sub> and C<sub>2</sub>H<sub>2</sub>-Ar irradiated with Ar<sup>+</sup>. At a deposition temperature of 400°C and postdeposition annealing up to 800°C under Ar flow, crystal growth and graphitization are obtained on Cu and Ni foils and interestingly on NaCl. Recently, the growth of Gr grains on Cu substrate using the radio frequency PECVD (RF-PECVD) at different temperatures has been reported [43]. These authors demonstrated the fabrication of large polycrystalline Gr grains at high temperatures and a relatively long dwell time. Large area Gr sheets of several mm<sup>2</sup> were synthesized on Cu substrates by this technique using a H<sub>2</sub>/CH<sub>4</sub> gas mixture [44]. Using PECVD, Yang et al. [45] demonstrated the direct growth of Gr walls on dielectric substrates and Hussain et al. [46] fabricated vertically aligned Gr at lower temperature and low power, while Chugh et al. [47] compared the growth of Gr on arbitrary noncatalytic substrates at low temperature. To summarize the various conditions of the Gr growth using PECVD technique, we have drawn up Table 2.

**2.3. Chemical and Green Synthesis.** Oxidative exfoliation of graphite was also used to synthesize GrO, which in turn was reduced to obtain Gr sheets. Brodie, Staudenmaier, and Hummers are the major methods to obtain Gr from the oxidative exfoliation-reduction (Figure 3).

Oxidation of graphite in the presence of graphite intercalation compounds increases the distance between graphite layers. This weakens the interlayer Van der Waals forces, which allows their exfoliation by sonication in the presence of suitable solvents. Single-layer GrO, dual-layer GrO, and few-layer GrO are thus obtained. This is followed by the reduction of GrO into Gr using hydrazine (N<sub>2</sub>H<sub>4</sub>). However, due to its toxicity and high cost, alternate methods were developed to replace the use of hydrazine. Among those methods, we cite thermal reduction, hydrothermal reduction, and electrochemical reduction. Besides, Gürnlü et al. reported on a green synthesis method of Gr at the temperature range of 500–800°C, in which Gr powder was mixed

with LiCl/KCl and subsequently heated under Ar or N<sub>2</sub> atmosphere in a steel reactor. The thickness of the synthesized Gr films was found to be in the range of 5 to 9 nm, which was attributed to the presence of few layers of Gr [48].

### 3. Synthesis of g-CN

Various elaboration techniques have been reported in the literature for the fabrication of g-CN. Methods such as CVD, physical vapor deposition (PVD), Radio Frequency Magnetron- (RFM-) based sputtering method, and sol-gel-based spin-coating deposition have been used most often. The various characteristics are listed and compared in Table 3.

The spin-coating method is a simple and efficient technique. The stability of the dispersion depends on many parameters, such as the type of solvent, the viscosity of the solvent, and the size of the particles. To increase the performance and quality of the thin film, it is necessary to avoid the agglomeration of the powder and to ensure that it is deposited evenly on the substrate to prevent the formation of holes [54]. PVD is one of the effective techniques for fabricating thin films and nanostructures with high optical and electronic properties. In the PVD process, the crucial step is to produce the vapor phase of the solid precursor. PVD has been successfully applied in the elaboration of many materials, including carbon nitride for nanotubes [55]. CVD method can synthesize ultrathin films and can be used in the fabrication of heterojunctions [56]. Reactive RFM-based sputtering technique is a technique capable of making large area films. However, this is a multiparameter process. The reactive sputtering process involves the use of a high purity target and plasma medium [52].

**3.1. Thermal Condensation Synthesis.** g-CN bulk crystal is easily prepared at large scale by thermal condensation of precursors rich in carbon and nitrogen such as thiourea (CH<sub>4</sub>N<sub>2</sub>S) [57], melamine (C<sub>3</sub>H<sub>6</sub>N<sub>6</sub>) [58], dicyandiamide (C<sub>2</sub>H<sub>4</sub>N<sub>4</sub>) [23], and urea (CH<sub>4</sub>N<sub>2</sub>O) [59] as schematically depicted in Figure 4.

Single-layered or multilayered g-CN nanosheets (NSs) are subsequently obtained through exfoliation of the bulk g-CN resulting in large active surfaces [58]. The bulk g-CN presents dense and thick layers due to the agglomeration of flat sheets of g-CN to build a massive, layered structure. Table 4 summarizes the various conditions for manufacturing g-CN under atmosphere.

Ismael et al. synthesized bulk g-CN from melamine, thiourea, and urea [61] and reported that bulk g-CN elaborated by melamine and thiourea contains smooth, thin, and large sheets. Meanwhile the sample elaborated by urea consists of smaller sheets and porous sheets. The exfoliation of bulk g-CN results in the formation of large, irregular-shaped, porous thin sheets, with a variable degree of flexibility [56, 62–64]. Iqbal et al. [65] synthesized mesoporous g-CN NSs by a simple one-step approach using glucose and NH<sub>4</sub> together with the chosen precursor for exfoliation of bulk g-CN.

TABLE 1: Comparison of various Gr preparation methods.

Method	Exfoliation	SiC epitaxy	CVD on Ni	CVD on Cu
Layers	1–10 [36]	1–4 [37]	1–4 [38]	Single [39]
Size	1 mm [36]	50 $\mu\text{m}$ [37]	1 cm [38]	65 cm [40]
Mobility ( $\text{cm}^2\text{V}^{-1}\text{s}^{-1}$ )	1500–10 <sup>6</sup> [41]	2000–11,000 [37]	3700 [38]	16,000–65,000 [40]
Synthesis temperature ( $^{\circ}\text{C}$ )	Room temperature	1000–1500	1000	1000
Cost	High	High	Low	Low
Scalability	Not possible	Good	Good	Good
Advantages	(i) Easy and low cost (ii) No special equipment is needed (iii) $\text{SiO}_2$ thickness is tuned for better optical contrast used for visual localization (iv) Large-scale area	(i) Graphene sheets of even thickness (ii) Large-scale area	(i) Morphology can be controlled by maintaining process parameters (ii) Large-scale production is easy	(i) Morphology can be controlled by maintaining process parameters (ii) Large-scale production is easy
Disadvantages	(i) Serendipitous (ii) Uneven films (iii) Non-scalable	(i) Difficult control of morphology (ii) High processing temperatures	(i) Uniform thickness is difficult (ii) Low deposition rates	(i) Uniform thickness is difficult (ii) Low deposition rates

TABLE 2: Parameters for the production of Gr by the PECVD technique.

Carbon source/flow rate (sccm)	Gas carrier/flow rate (sccm)	Substrate	Substrate/annealed temperature ( $^{\circ}\text{C}$ )	Time (s)	Power (KW)	RF power (MHz)	Ref.
$\text{C}_2\text{H}_2/15$	Ar/5	Si, Si/ $\text{SiO}_2$ , Ni, Cu, MgO, NaCl, glass	Ambient to 400/800	—	—	—	[42]
$\text{CH}_4/8$	Ar/30 and $\text{H}_2/10$	Cu	670–850	10–90	0.050	—	[43]
$\text{CH}_4/25$	$\text{H}_2/200$	Cu	900	600	1	—	[44]
$\text{CH}_4/5$	$\text{H}_2/20$	$\text{SiO}_2$	900	3600	0.300	13.56	[45]
$\text{C}_2\text{H}_4/20$	$\text{H}_2/40$	Si/Al	450/(450 to 620)	900	0.030	13.56	[46]
$\text{CH}_4/6$	Ar/5	$\text{SiO}_2$ , quartz	650	900	-	13.56	[47]

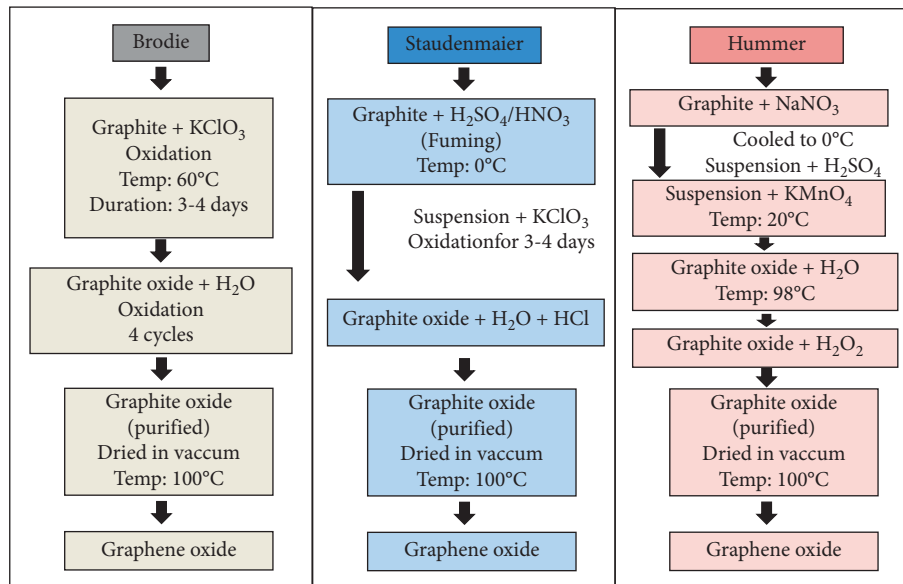


FIGURE 3: Schematic of various methods of exfoliation by oxidation.

TABLE 3: Advantages and disadvantages of different techniques employed for the fabrication of g-CN films.

Techniques	Advantages	Disadvantages	Ref.
Spin-coating	(i) Large surface area (ii) Highly adhesive (iii) Easiest, homogeneity (iv) Appropriate for deposition on any substrate	(i) High cost for the fabrication (ii) High cost of precursors (iii) Needed controlled atmosphere	[49, 50]
CVD	(i) High deposition rate (ii) Uniform film (i) High quality and uniform films, simply controlled sputtering speed, good adhesion	(i) Low deposition rates	[49, 51]
RFM-based sputtering deposition	(ii) Useful manipulation, offers large area coatings (iii) Uniform coating thickness. Compact, pore-free coating. Capability to coat on heat-sensitive substrates	(i) Plasma damage (ii) Plasma contamination (iii) Probability of substrate damage due to ionic bombardment	[49, 52]
PVD	(i) Low hydrogen content	(i) Low deposition rate (ii) Difficult to control film thickness	[51, 53]

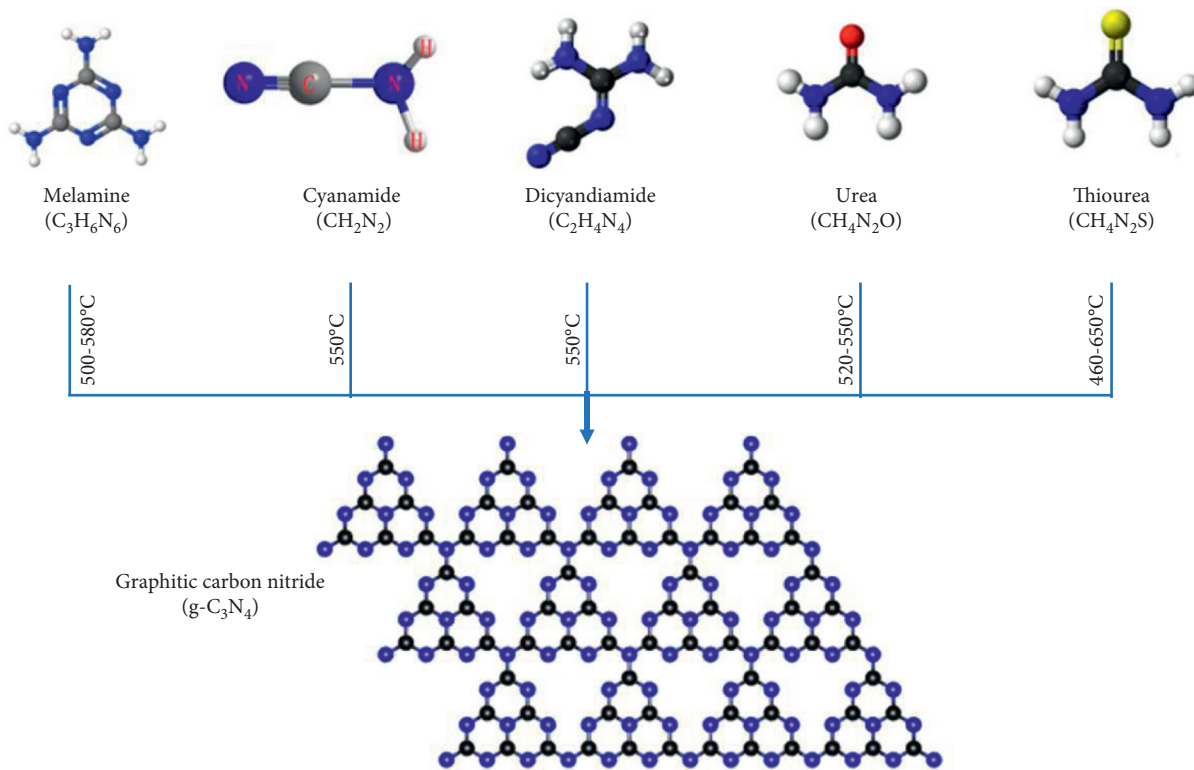


FIGURE 4: Synthesis processes of g-CN by thermal condensation of different precursors (reproduced and adapted from [60]).

TABLE 4: Various conditions for manufacturing g-CN under air atmosphere with thermal condensation.

Precursors	$T$ ( $^{\circ}\text{C}$ )	$t$ (h)	Heating rate (K/min)	Ref.
Urea	520	0.5	—	[54]
Dicyandiamide	550	4	20	[52]
Dicyandiamide	550	4	2.2	[23]
Melamine	520	5	5	[58]
Melamine	530	2	5	[25]

**3.2. Chemical Vapor Deposition.** For the synthesis of g-CN films by the CVD method, generally a precursor rich in C and N is placed at the inlet of an Ar gas stream in a quartz tube that is maintained at low pressure. The powder

vapors penetrate inside the hot zone of the furnace ( $600^{\circ}\text{C}$ ), due to the flow of Ar gas with the low vacuum inside the quartz tube. Condensation of the precursor at high temperature produces the g-CN structure. After deposition, the furnace should be allowed to cool to room temperature automatically in Ar environment [66]. Table 5 summarizes the conditions for depositing g-CN using the CVD technique.

Similarly, plasma-enhanced chemical vapor deposition (PECVD) allows the deposition of thin layers of material on different types of substrates (glass, Si, etc.), after decomposition of the molecules of the reactive gases in a plasma. Table 6 shows the conditions for depositing g-CN using the PECVD technique.

TABLE 5: The deposition conditions of carbon nitride by CVD technique.

Precursors	Atmosphere	$T$ ( $^{\circ}\text{C}$ )	$t$ (h)	Heating rate (K/min)	Shape	Ref.
Melamine and thiourea	Air	550	4	2	—	[51]
Melamine	—	550	3	—	Flakes	[67]
Dicyandiamide	Ar	600	—	—	Films	[66]

TABLE 6: The deposition conditions of carbon nitride by PECVD technique.

Carbon source/ flow rate	Nitrogen source/ flow rate	Carrier gases/flow rate	Substrate temperature ( $^{\circ}\text{C}$ )	Deposition time	Power (W)	RF power (MHz)	Ref.
$\text{C}_2\text{H}_4/0.5$ L/min	$\text{N}_2/3$ L/min	$\text{H}_2/4$ sccm	400	6 h	840	—	[68]
$\text{C}_6\text{H}_6/—$	$\text{N}_2/10$ sccm	$\text{H}_2/5$ sccm	RT to 200	—	60	13.56	[69]

#### 4. Characterization of g-CN

The characterization of g-CN by molecular vibrational spectroscopy (FTIR) basically reveals specificities of g-CN. The transmission spectrum of bulk g-CN in the wavelength range of  $500\text{--}4000\text{ cm}^{-1}$  is shown in Figure 5.

The peaks at  $802\text{ cm}^{-1}$  and  $889\text{ cm}^{-1}$  correspond to the presence of s-triazine units in g-CN, caused by the bending vibration of the triazine ring. The peaks in the range of  $1200$  to  $1700\text{ cm}^{-1}$  are attributed to the stretching vibration of the aromatic heterocyclic units of heptazine ( $\text{C}_6\text{N}_7$ ). The smaller peaks observed at  $1250$ ,  $1320$ ,  $1419$ , and  $1457\text{ cm}^{-1}$  are related to the stretching vibrations of the C-N bonds, while the peak appearing at  $1612\text{ cm}^{-1}$  relates to the stretching vibration of the C=N bond in heptazine units. The large absorption band centered at  $3124\text{ cm}^{-1}$  corresponds to the stretching vibration of the N-H bond to NH and  $\text{NH}_2$  groups present at the end of g-CN, indicating that g-CN was undergoing incomplete polycondensation [65, 71]. Guigoz et al. [72] reported that the FTIR spectrum of g-CN NSs exhibits the same distinctive main bands, signature of the g-CN bulk.

X-ray photoelectron spectroscopy (XPS) indicates the presence of two main elements (carbon, C, and nitrogen, N) with two predominant peaks of C1s and N1s (Figure 6).

At high-resolution XPS spectrum of C1s, the peak is deconvoluted into three different components with binding energies at  $284.6$ ,  $286.0$ , and  $288.1\text{ eV}$  corresponding to functional groups of graphitic carbon [74]. The first component is assigned to C-C or C=C bonds, and the second is identified as a carbon bonded to nitrogen atoms in aromatic rings [C-(N)<sub>3</sub>], while that at  $288.1\text{ eV}$  is assigned to the (N-C=N) bonds. The high resolution of N1s spectrum exhibits three components around  $398.3\text{ eV}$ ,  $399.9\text{ eV}$ , and  $400.6\text{ eV}$ . The peak at  $398.3\text{ eV}$  is attributed to N binding to carbon atoms involved in triazine units (C-N=C), while the peak at  $399.9\text{ eV}$  is assigned to tertiary nitrogen groups N-@<sub>3</sub>. These last two peaks constitute the heterocyclic ring units of tri-s-triazine, constructing g-CN. The third peak at  $400.6\text{ eV}$  indicates the presence of amino functions (C-N-H), resulting from the incomplete condensation of the structures of the melon [57].

The elemental composition, their atomic percentages, and the carbon/nitrogen atomic ratio (C/N) in g-CN are

shown in Table 7 [75]. A smaller percentage of oxygen formed at the samples' surfaces is found with the ratio of C/N often at  $0.73$  [75].

The molecular vibration properties of g-CN examined by Raman spectroscopy under UV illumination reveal several characteristic peaks corresponding to the vibrational modes of CN heterocycles (Figure 7(a)). Similar trends are obtained using the Cambridge Sequential Total Energy Package (CASTEP) code implemented using density functional theory (DFT) (Figure 7(b)) [76].

This confirms the results of experimental Raman spectroscopy. Interestingly, the comparison of the bulk and single layer of g-CN theoretical Raman spectra shows that the characteristic bands remain visible in both cases, indicating that the exfoliation treatment does not cause any damage to the g-tri-s-triazine-CN. Only a decrease in intensity for the nanosheets is observed, which is attributed to the low-dimensional character. Nonetheless, a small shift is observed for the N-C ( $\text{sp}^2$ ) bending vibration peak at  $1224\text{ cm}^{-1}$  for the bulk sample, which is displaced to  $1232\text{ cm}^{-1}$  in g-CN NSs. This originates from phonon confinement and strong quantum confinement effects [76]. The second characteristic is related to the peak height ratios of  $583\text{--}478\text{ cm}^{-1}$  ( $I_{583}/I_{478}$ ) and  $761\text{--}704\text{ cm}^{-1}$  ( $I_{761}/I_{704}$ ), equivalent to the layer-layer strain vibrations or the correlating vibrations induced by the layer-layer vibrations. It is found that these ratios tend to increase with the decreasing number of g-CN layers.

The XRD diagrams depicted in Figure 8 show two diffraction peaks at  $13.0^{\circ}$  and  $27.2^{\circ}$ . The large peak (002) at  $2\theta = 27.2^{\circ}$  is the peak characteristic of the interlayer stacking of an aromatic cyclic system of graphitic type. The much smaller peak (100) at  $2\theta = 13.0^{\circ}$  is characteristic of tri-s-triazine repeating units in melon-like materials [71, 77]. Its unchanged position in the g-CN NSs revealed that the chemical exfoliation has no impact on the aromatic cyclic structure of g-CN.

The intensity reduction of (002) peak observed in nanosheets is a signature of successful exfoliation of g-CN. It is worth noting that the diffraction peak at  $13.0^{\circ}$  is also decreased compared to the g-CN bulk, which is likely due to the reduced planar size after exfoliation step. The calculated interplanar distance of the aromatic series is  $d = 0.33\text{ nm}$ , indicating a layered-like structure similar to crystalline

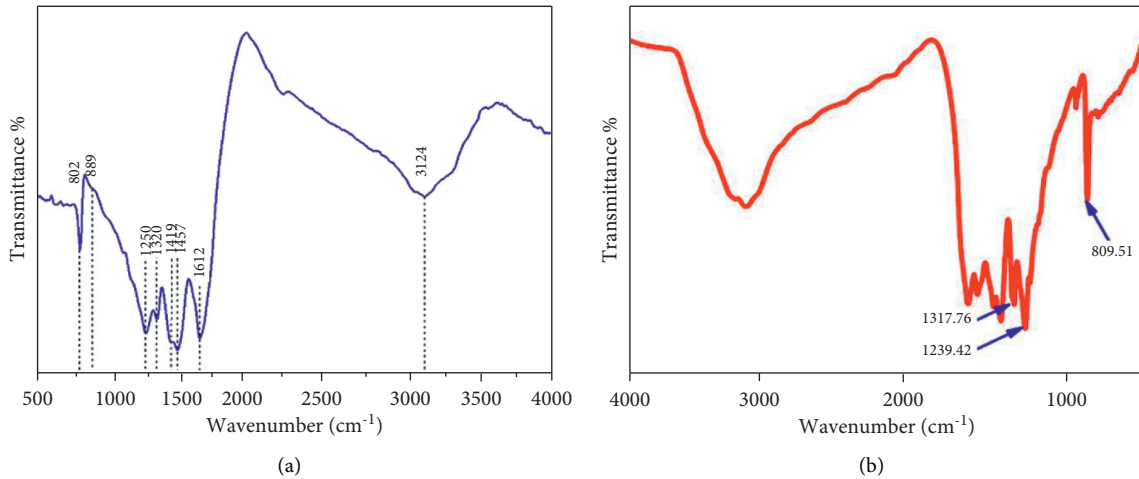


FIGURE 5: FTIR spectra of (a) bulk g-CN and (b) g-CN NSs (reproduced and adapted from [70]).

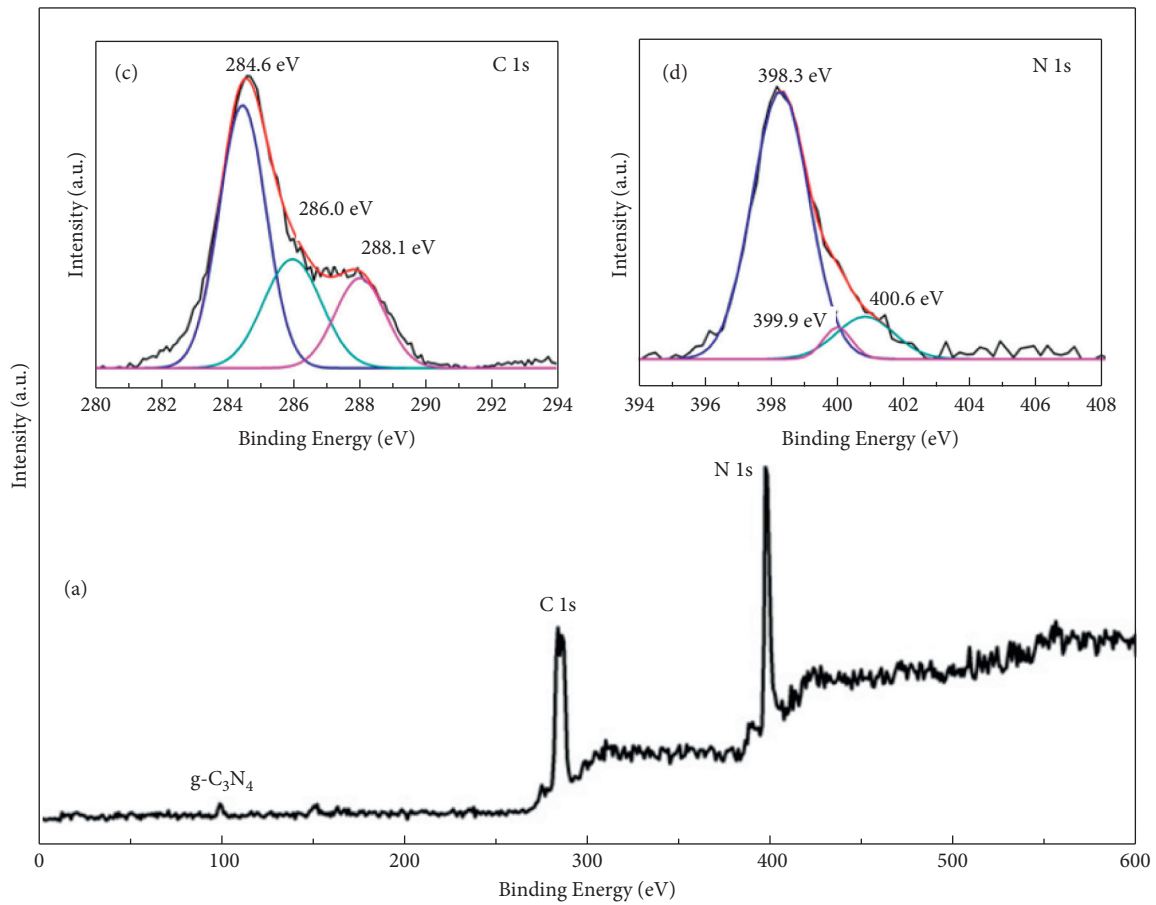


FIGURE 6: XPS spectra of g-CN (reproduced and adapted from [73]).

TABLE 7: Percentage of atomic composition obtained from XPS analysis.

	C	N	O	C/N
Atomic concentration %	41.18	56.58	2.24	0.73

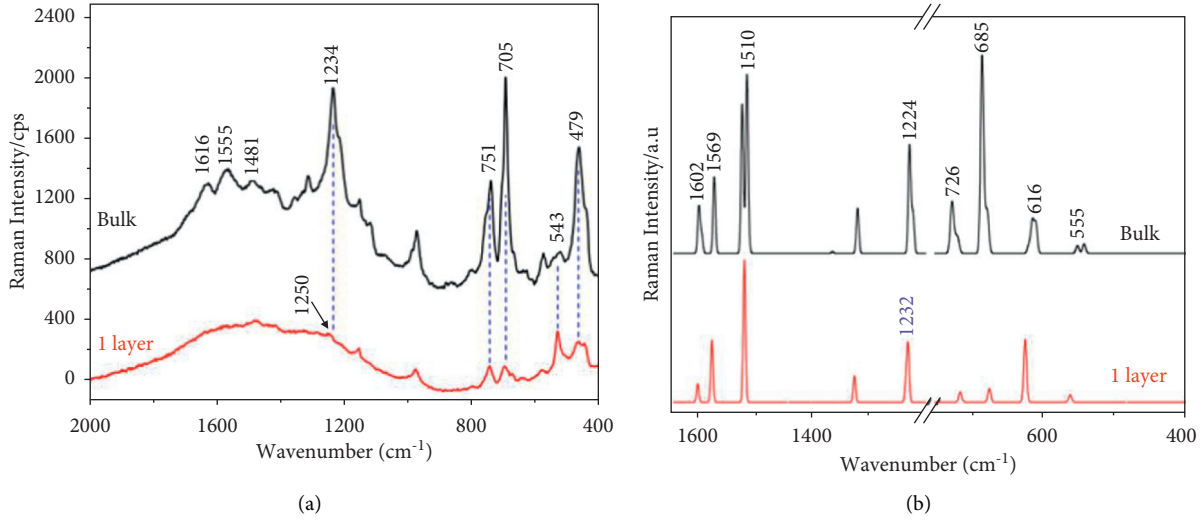


FIGURE 7: (a) Experimental Raman spectra of bulk and signal-layer g-CN and (b) calculated Raman spectra of bulk and signal-layer g-CN (reproduced from [76]).

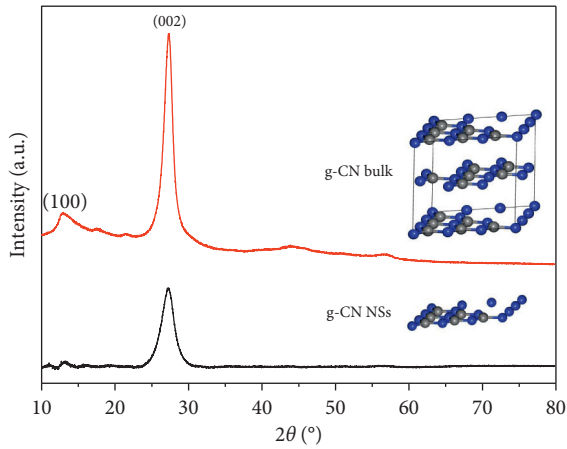


FIGURE 8: XRD patterns of bulk g-CN and g-CN NSs.

graphite ( $d=0.335$  nm) [78]. This result suggests a typical g-CN structure [79]. Both NSs and bulk g-CN show strong emission peaks, respectively, at 445 nm and 464 nm when exposed to visible light excitation using a photoluminescence experimental setup. These peaks correspond to the band gap energies of 2.78 eV and 2.67 eV for the NSs and bulk g-CN, respectively [54, 62, 74, 80].

The optical band deviation ( $E_g$ ) was also estimated from absorbance measurements using the Tauc model [71, 81]:

$$(\alpha h\nu) = B(h\nu - E_g)^m, \quad (1)$$

where  $\alpha$  is the absorption coefficient,  $h\nu$  is the photon energy,  $E_g$  the optical band gap,  $B$  is a constant, and  $m$  is an exponent that characterizes the optical absorption process. For the direct authorized transition  $m = 1/2$ , for the indirect authorized transition  $m = 2$ , for the direct forbidden transition  $m = 3/2$ , and for the indirect forbidden transition  $m = 3$ .

The plotting of  $[(\alpha h\nu)^{1/m}]$  as a function of the energy of the photon ( $h\nu$ ) and the extrapolation of the linear part of

the curve to  $[(\alpha h\nu)^{1/m} = 0]$  on the energy axis provides the value of the optical band gap ( $E_g$ ). The value of  $m = 1/2$  is suitable for g-CN because it has a direct allowed band gap [74]. By using the Tauc model, Huang et al. [56] found the band gaps for bulk g-CN and g-CN NSs to be approximately 2.72 eV and 2.82 eV, respectively. They attributed this increase in the band gap energy from bulk to nanolayers by the effect of quantum confinement.

## 5. Gas-Sensing Investigations

**5.1. Gas-Sensing Mechanisms.** The physical principle of a gas sensor is based on charge transfer process, in which the detection material acts as a charge donor or a charge acceptor [5, 16, 34, 82]. Upon exposure to different gases, the charge transfer reaction occurs in different directions between the sensing material and the adsorbed gases, which leads to different changes in the resistance of the material [83]. In absence of adsorbed gas molecules, or upon reexposure to air, the original resistance of the material is recovered. Figure 9 shows a schematic that describes the change of resistance related to charge transfer processes from adsorbed gases. Considering an n-type material exposed to an electron donor gas (reducing gas), electrons are transferred from the gas molecules to the n-type material causing an increase in the density of majority of charge carriers (electrons). Consequently, the resistance of the n-type material decreases. Seemingly in the case of an n-type material exposed to an acceptor gas (oxidizing gas), the electrons are transferred from the material to the gas molecules resulting in a decrease of the majority of charge carriers' density in the material. As a result, the resistance of the n-type material increases.

Similar processes occur in the case of a p-type material. Its exposure to a reducing gas causes electron to transfer from the gas molecules to the material, hence decreasing the density of the majority of charge carriers (holes) in the p-type material and resulting in a decrease of the p-type

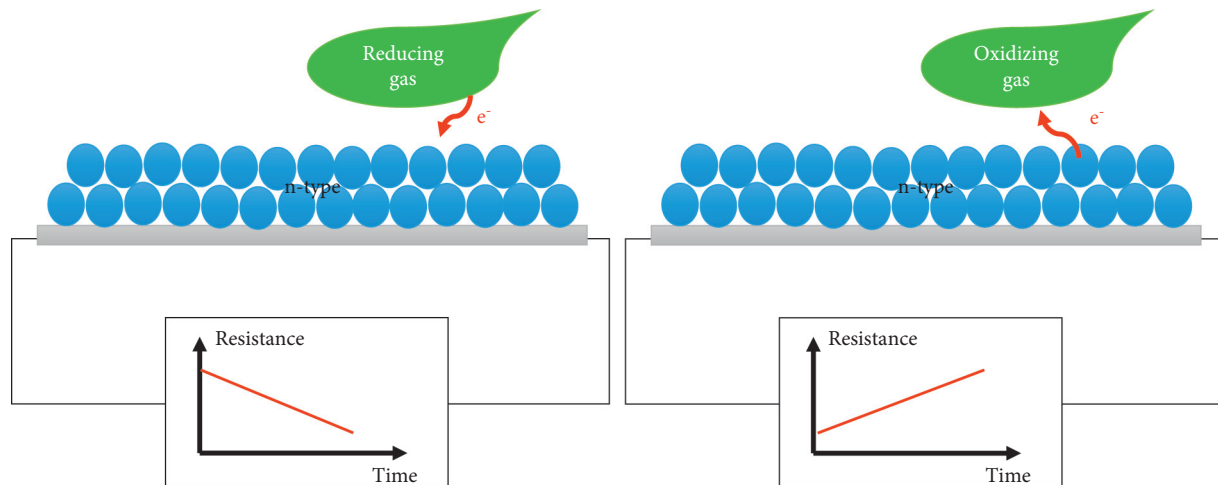


FIGURE 9: The detection mechanism of an n-type gas sensor.

material's resistance. In contrast, if the adsorbed gas is oxidizing, electrons are transferred from the material to the gas molecules, resulting in an increase of the charge carriers' density in the material. As a result, the resistance of the p-type material decreases.

**5.2. Graphene-Sensing Performance.** Studies have proved that defects and dopants in Gr increase its gas sensitivity considerably [84–87]. Modification of Gr with boron, nitrogen, and defect increases its adsorption energy with gases such as ammonia, as well as oxides of nitrogen and carbon [84]. Doping Gr with metals such as Mg, Co, Fe, and Ni increases sensitivity of Gr for gases such as  $\text{H}_2\text{S}$ ,  $\text{SO}_2$ , and  $\text{O}_2$ . Table 8 shows sensing characteristics of various dopants with Gr for various gases.

Microsensors made of mechanically exfoliated Gr are capable of sensing even single molecules of  $\text{NO}_2$  in high vacuum [21]. The adsorption of electron accepting molecules such as  $\text{NO}_2$  and  $\text{H}_2\text{S}$  onto Gr leads to a decrease of its resistivity due to an increase in holes concentration. Meanwhile, electron donor molecules such as CO and  $\text{NH}_3$  increase resistivity of Gr when adsorbed to it, which is due to increase in electron concentration as shown in Figure 10.

A 3.5–5 nm thick mechanically exfoliated Gr used as a gas sensor has shown commendable sensitivity, reproducibility, and selectivity in response to  $\text{NO}_2$  at 100 ppm as shown in Figure 11. Sensors based on CVD made Gr show significant sensitivity to various gases at a minimum concentration of 1 ppq [90]. Schottky diode sensors made of Gr/n-si have proven to be potential  $\text{H}_2\text{S}$  gas-sensing device [91].

Graphene oxides (GrO) are promising gas-sensing materials owing to their oxygen-rich functional groups. Single-layer to few-layer GrO (dimensions ranging from 27 to 500  $\mu\text{m}$ ) based sensors fabricated by drop casting show a p-type response in both oxidizing and reducing environments [92]. GrO based sensors fabricated by dielectrophoresis are used to sense hydrogen gas [93]. GrO with acoustic wave propagated surface is used to detect  $\text{H}_2$  and  $\text{NO}_2$  in the atmosphere [94, 95]. Dense functional groups of

oxygen in GrO maintain its sensitivity even in harsh conditions such as high humidity and strong acidic or basic conditions and also sense harsh volatile content like chloroform [96].

Reduced graphene oxide (r-GrO) is widely used in sensing gases. r-GrO is preferred over Gr due to its low cost and tailorable structure and properties [22]. The enhancements in the r-GrO response to gases are associated with the carbon atoms, holes, or vacancies created due to thermal treatments. Sensors fabricated by r-GrO (made by annealing of GrO at 300°C) show conductance that is 4.3% more than that of mechanically exfoliated Gr [21]. Cost-effective gas sensors based on r-GrO were fabricated on paper substrates to sense  $\text{NO}_2$  at lower ppm levels. It is also noted that sensing behavior depends on both the thickness and size of the r-GrO flakes [97]. The poor selectivity of Gr constitutes one main drawback for its usage in gas-sensing devices. Nevertheless, its functionalization with metallic or metal oxide nanoparticles has been shown to enhance its selectivity [98–102]. In fact, pristine Gr shows insignificant change in resistance when hydrogen gas molecules are adsorbed onto it. Meanwhile, nano-Pd decorated Gr shows considerable changes in resistance because Pd hydride on the surface of Gr donates more electrons [99]. r-GrO decorated with palladium can sense NO from 2 to 420 ppb. r-GrO functionalized with  $-\text{SO}_3\text{H}$  and decorated with nano-Ag showed a superior performance in measuring  $\text{NO}_2$  and  $\text{NH}_3$  gases [102, 103]. Table 9 shows details of gases sensed by different Gr decorated by various nanoparticles.

Regardless of its comparison with g-CN, Gr remains an interesting 2D material suitable for gas sensing due to its large specific surface area, high carriers' mobility, high sensitivity, fast response, low power consumption, and its operation under ambient conditions [120]. Moreover, when Gr is associated with perovskites [121], polymers [122], or organic molecules [123], its sensing performance was found to be improved at room temperature. Indeed, the composite form of Gr, whether with a polymer or a perovskite or organic molecules, provides specific reaction sites for gas adsorption, hence improving the sensor selectivity at room

TABLE 8: Characteristics of graphene with dopants.

Ref.	Gas	Dopant	Minimum concentration (ppt)	Detection limit (ppt)	Theoretical adsorption energy ( $E_{ad}$ ) (eV)	Theoretical Mulliken charge (Q) (e)
[86, 87]		Pristine	10	0.158	0.029	0.018
[82]	NO	Pristine	—	—	-0.30	0.04
[82]		Boron	—	—	-1.07	0.15
[82]		Nitrogen	—	—	-0.40	0.01
[86, 87]		Pristine	20	2.06	0.067	-0.099
[82]	NO <sub>2</sub>	Pristine	—	—	-0.48	-0.19
[82]		Boron	—	—	-1.37	-0.34
[82]		Nitrogen	—	—	-0.98	-0.55
[86, 87]		Pristine	200	33.2	0.031	0.027
[82]	NH <sub>3</sub>	Pristine	—	—	-0.11	0.02
[82]		Boron	—	—	-0.50	0.40
[82]		Nitrogen	—	—	-0.12	0.04
[87]	N <sub>2</sub> O	Pristine	200	103	—	—
[87]	O <sub>2</sub>	Pristine	200	38.8	—	—
[86]		Pristine	—	—	0.014	0.012
[82]	CO	Pristine	—	—	-0.12	-0.01
[82]		Boron	—	—	-0.14	-0.02
[82]		Nitrogen	—	—	-0.14	0
[87]	CO <sub>2</sub>	Pristine	200	136	—	—
[82, 87]	SO <sub>2</sub>	Pristine	200	67.4	0.012	-0.077
[83]		Boron	—	—	0.205	-0.110

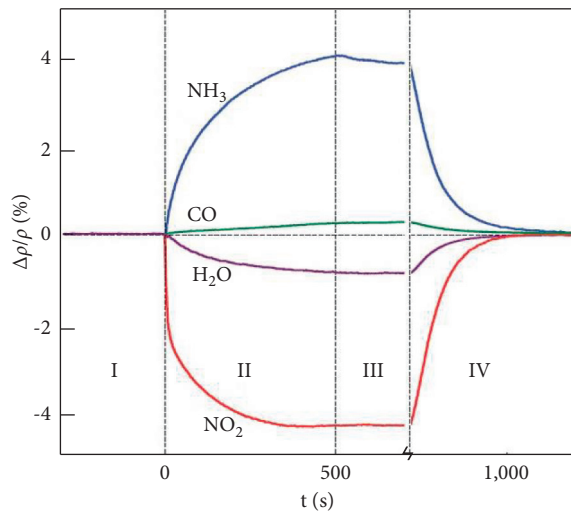


FIGURE 10: Change in resistivity when Gr is exposed to various gases [88].

temperature. When Gr was used in conjunction with g-CN [124], g-CN showed superior performance compared to Gr in both gas sensing and catalysis, which was attributed to the increased interaction sites offered by 2D g-CN structure.

**5.3. g-CN Sensing Performance.** Several works have been reported on the influence of the g-CN content on its gas-sensing performances. Karthik et al. [103] reported that thin layers (elaborated by a spray pyrolysis) of TiO<sub>2</sub> porous nanospheres decorated with g-CN showed excellent detection performance of CO<sub>2</sub> gas with very fast response and recovery. The results show that 10 wt.% g-CN decorated TiO<sub>2</sub> composite layer exhibits an exceptional detection

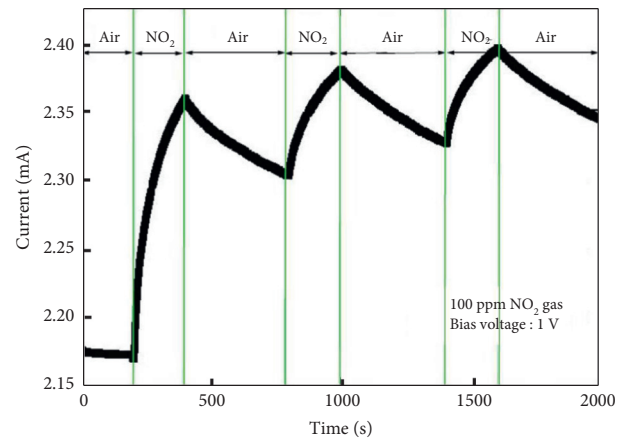


FIGURE 11: Reversibility of gas sensors [89].

response of 88% and a great stability for CO<sub>2</sub> gas at 450°C under 1500 ppm. The enhanced detection response is attributed to the increased surface area of 108.5 m<sup>2</sup>/g due to the porous nature of g-CN (15.7 nm). Zhang et al. [58] showed that gas detection properties such as gas selectivity and sensitivity of SnO<sub>2</sub> to acetic acid as well as the operating temperature were enhanced by the incorporation of g-CN into SnO<sub>2</sub>. Their results indicate that the operating temperature for the detection of acetic acid was decreased from 230°C to 185°C. In particular, the g-CN-SnO<sub>2</sub> nanocomposite-based gas sensor containing 10% by weight of g-CN revealed the highest sensitivity of 87.7 to 1000 ppm acetic acid, the fastest response, lower recovery time, and the lowest detection limit down to 0.1 ppm. Besides, calcination temperatures, calcination times, and precursor ratios were also reported to significantly affect the performance of sensors to target gases. For example, Hu et al. [14] have

TABLE 9: Sensitivity of metal nanopowders decorated graphene sensors.

Ref.	Gas	Nanometal-Gr	Sensitivity (%)	Response time (min)
[97]		Pd-Gr	$\Delta R = 5$	1.0
[98]		Pd-gr	$\Delta R = 33$	1
[99]		Pt-gr	$\Delta R = 3$	—
[104]	H <sub>2</sub>	Pt-gr	$\Delta V = 66.1$	1.25
[105]		ZnO-GrO	$\Delta R = 250$	0.35
[106]		Pd-WO <sub>3</sub> -rGrO	$\Delta G = 7200$	0.59
[107]		Pt-rGrO	$\Delta V = 22$	—
[108]		SnO <sub>2</sub> -gr	$\Delta R = -6$	3.15
[109]		WO <sub>3</sub> -gr	$\Delta R = 96$	0.42–3.3
[110]		CNT-GrO	$\Delta R = 20$	60
[111]	NO <sub>2</sub>	NiO-GrO	$\Delta R = 200$	—
[112]		ZnO-GrO	$\Delta R = 25.6$	2.75
[113]		CO <sub>3</sub> O <sub>4</sub> -GrO	$\Delta R = 80$	<1–2
[114]		SnO <sub>2</sub> -rGrO	$\Delta R = 231$	2.25
[115]		WO <sub>3</sub> -rGrO	$\Delta R = 102$	—
[116]		SnO <sub>2</sub> -gr	$\Delta R < 60$	0.26
[117]	CO <sub>2</sub>	Al <sub>2</sub> O <sub>3</sub> -gr	$\Delta R = 1084$	0.24
[116]		Sb <sub>2</sub> O <sub>3</sub> -gr	$\Delta R < 60$	0.26
[118]	LPG	Bi <sub>2</sub> O <sub>3</sub> -gr	$\Delta R = 400$	0.26
[119]		MnO <sub>2</sub> -rGrO	$\Delta R = 50$	0.27

examined the effect of elaboration conditions on the detection performance of g-CN-SnO<sub>2</sub> nanocomposites using 500 ppm acetone as the target gas. The 200/100 ratio between melamine and SnCl<sub>2</sub> · 2H<sub>2</sub>O and the calcination for 3 hours at 500°C appeared to offer better detection properties. For instance, these preparation conditions enhanced the detection sensitivity 22 times compared to pure SnO<sub>2</sub> at a fast response and recovery time (7 s/8 s) while achieving very low detection limit of 67 ppb. In addition, the element ratios (melamine and SnCl<sub>2</sub> · 2H<sub>2</sub>O) were also used to determine the important role of g-CN in the g-CN-SnO<sub>2</sub> nanocomposite sensor. In parallel, Absalan et al. [25] have synthesized CO gas sensors based on Pd/SnO<sub>2</sub>/g-CN nanocomposites by the hydrothermal method at different Pd and g-CN contents. The nanocomposites made of 5% Pd/SnO<sub>2</sub>/5% g-CN presented remarkable CO detection capabilities such as good selectivity and stability, superior response, short response, and low recovery times at very low operating temperature of 125°C. The exceptional gas detection performances of these nanocomposites were attributed to the large specific surface area of g-CN. Similarly, Chu et al. [125] examined the g-CN-WO<sub>3</sub> composite synthesized by hydrothermal treatment. Their results revealed that adding a suitable quantity of g-CN to WO<sub>3</sub> was found to enhance the selectivity and sensitivity to acetone vapor. The sensor based on 2 wt% g-CN-WO<sub>3</sub> composite, at an ideal operating temperature of 310°C, presented a response to 1000 ppm acetone of Ra/Rg = 58.2. Moreover, Zhang et al. [126] studied g-CN/MgFe<sub>2</sub>O<sub>4</sub> composites synthesized by a one-step solvothermal process as acetone gas sensor. The gas detection properties of the models were determined and compared to a sensor based on pure MgFe<sub>2</sub>O<sub>4</sub>. The higher sensing performance was achieved at 10 wt% g-CN content, where the sensitivity to acetone was enhanced by approximately 145 times, while the best possible operating

temperature was 320°C. The MgFe<sub>2</sub>O<sub>4</sub>/g-CN-10wt% based sensor exhibits outstanding acetone detection performance, high sensitivity and selectivity, rapid response, and low recovery time and thus favorable stability.

Additionally, the gas sensors based on chemically exfoliated g-CN NSs were found to exhibit very low detection limits and ultrahigh sensitivity towards NO<sub>2</sub> gas compared to Gr as reported by Hang et al. [127]. Precisely, 15 wt% of g-CN NSs associated with Gr showed a better response than the sole Gr based sensor towards NO<sub>2</sub> gas. Similar gas-sensing enhancement was reported to occur for other compounds associated with g-CN such as ZnO/g-CN composite [128]. For instance, when ZnO/g-CN composite was irradiated with 460 nm light, it displayed the maximum response of 44.8 under 7 ppm of NO<sub>2</sub>, with a response and recovery times of 142 s and 190 s, respectively, and a detection limit of 38 ppb.

Table 10 summarizes the g-CN based nanocomposites for gas sensor applications including their characteristics, elaboration methods, and gas-sensing performances.

All aforementioned gas-sensing performances did not include specific sensing conditions that greatly influence the detection capabilities such as the relative humidity or mixed gases. In fact, humidity is a key factor that needs to be taken into account when analyzing the gas-sensing performances. For instance, the responsivity of g-CN gas sensors towards NO<sub>2</sub> was found to be altered in the presence of high levels of water vapor (about 90%) as shown in Figure 12(a) [129]. The sensing performance was decreased by 3 times for 90% RH compared to 50% RH.

Hence, the presence of humidity might compromise the detection of target gases. This result has to be considered with special care as this limitation is commonly overcome by increasing the operating temperature; this implies that the gas sensors need to be stable at intermediate temperatures while keeping their gas sensitivity unchanged. As an example of the sensing selectivity, Figure 12(b) is provided to illustrate the gas selectivity of g-CN sensors towards several common gases, where the highest selectivity was obtained on NO<sub>2</sub>.

## 6. Simulated Gas-Sensing Performances

Theoretical calculations show the adsorption energies between selected gas molecules (CO<sub>2</sub>, NO<sub>2</sub>, and HF) and g-CN monolayer. The comparison with Gr and r-GrO is shown using HF as a selected adsorption gas. The first-principles calculations are based on the density functional theory (DFT) using generalized gradient approximation (GGA) with the Perdew-Burke-Ernzerhof (PBE) exchange-correlation functional [81, 130], implemented in Quantum Espresso code [131]. In the optimized process, the vacuum spaces of 15 Å were set for the three compounds to separate the interactions between the layers. A (3 × 3 × 1) k-point was used in the structure optimization and total energy calculations. To study the stability of g-CN, Gr, and r-GrO surfaces with considered gas molecules, the adsorption energy of system was computed using the following relation [132, 133]:

TABLE 10: The performances of nanocomposites based on g-CN for gas sensor applications.

Material	Method	Response/Gas	Response/recovery time (s)	ppm level	Operation T (°C)	Detection limit	Comment	Ref.
TiO <sub>2</sub>		Ra/Rg = 25%/H <sub>2</sub> S	~52/60					
		Ra/Rg = 22%/CO <sub>2</sub>	45/55					
g-CN (10 wt %)/TiO <sub>2</sub>	Spray pyrolysis technique	Ra/Rg = 67%/H <sub>2</sub> S	~30/52	1500	450	U	The improvement in the detection performance of the sensor is due to the introduction of 10% of the g-CN nanosheets	[103]
		Ra/Rg = 88%/CO <sub>2</sub>	35/27					
SnO <sub>2</sub>		Ra/Rg = 13.4%/acetic acid	94/160		230°C	U	Improvement of the operating temperature and the sensitivity by introduction of 10 wt% of g-CN in SnO <sub>2</sub>	[58]
10 wt% of g-CN-SnO <sub>2</sub>	Hydrothermal method	Ra/Rg = 87.7%/CH <sub>3</sub> COOH	U	1000	185°C	0.1 ppm		
g-CN-SnO <sub>2</sub>	One-step calcination method	Vg/Va = 83%/acetone	7/8	500	380°C	67 ppb	A significant improvement in sensor performance by calcining melamine/SnO <sub>2</sub> powder for 3 hours	[14]
5%Pd/SnO <sub>2</sub> /5%g-CN	Hydrothermal method	(Rg-Ra)/Ra = 90.5%/CO	10/13	1000	125°C	75 ppm	g-CN-5% nanosheets with SnO <sub>2</sub> nanoparticles effectively improved the response of the gas sensors towards CO	[25]
2 wt% g-CN-WO <sub>3</sub>	Hydrothermal method	Ra/Rg = 58.2%/acetone	53/29	1000	310°C	0.5 ppm	A gas sensor based on 2% g-CN composite shows a higher response to acetone than pure WO <sub>3</sub>	[125]
10 wt% g-CN/MgFe <sub>2</sub> O <sub>4</sub>	One-step solvothermal method	Ra/Rg = 275%/acetone	49/29	500	320°C	30 ppb	The introduction of 10% of g-CN nanosheets in MgFe <sub>2</sub> O <sub>4</sub> improves their detection performance	[126]
Gr/g-CN	Drop coating method	(Rg-Ra)/Ra = 42%/NO <sub>2</sub>	U	5	100°C	600 ppb	Graphitic carbon nitride nanosheets with 15% of g-CN exhibit high detection performance compared to bulk g-CN and pure graphene	[127]
10 wt% g-CN/ZnO	Synthesized via ultrasonic mixing and subsequent calcination process	Rg/Ra = 44.8%/NO <sub>2</sub>	142/190	7	U	38 ppm	Detection performance is activated by LED light sources. 460 nm LED (12.7 W/m <sup>2</sup> )	[128]

"U": unavailable citation; it is not cited in the study. Vg/Va: electric voltages in the target gases and atmospheric air, respectively. Ra/Rg: electric resistances in the atmospheric air and target gases, respectively.

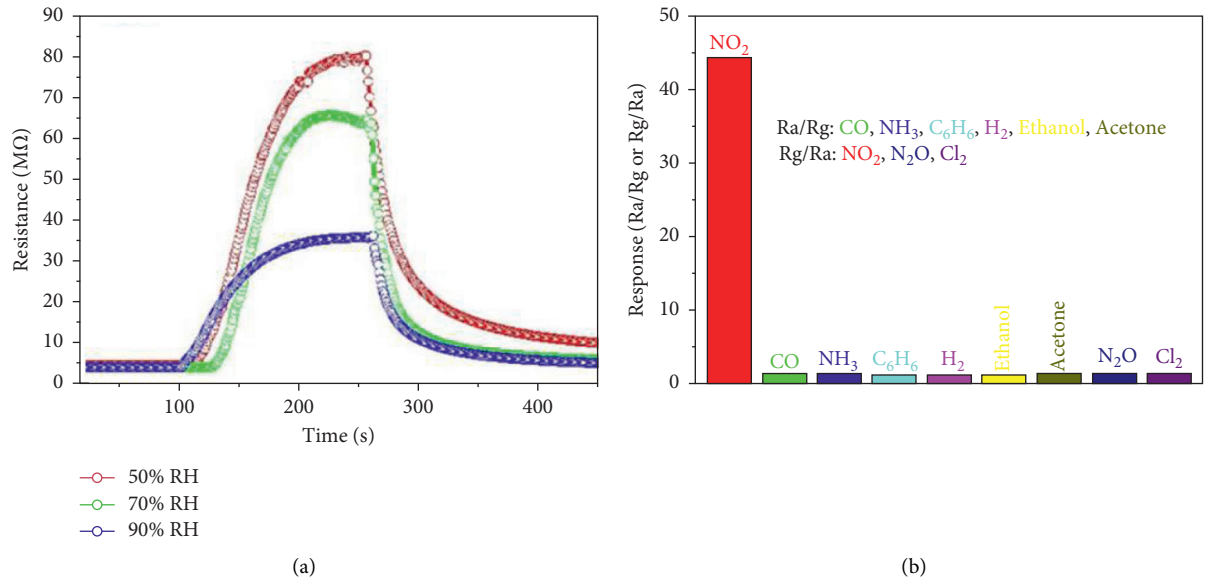


FIGURE 12: (a) Humidity effect on the response of gas sensors based on g-C<sub>3</sub>N<sub>4</sub> to 3 ppm NO<sub>2</sub>; (b) gas selectivity of g-C<sub>3</sub>N<sub>4</sub> sensors towards several common gases [129].

TABLE 11: Side and top views of the equilibrium adsorption configuration of NO<sub>2</sub>, CO<sub>2</sub>, and HF on g-CN and HF adsorbed on Gr and r-GrO.

Systems	Structure before optimization	Optimized structure
g-CN-NO <sub>2</sub>		
g-CN-CO <sub>2</sub>		
g-CN-HF		
r-GrO-HF		
Gr-HF		

TABLE 12: The angle between the bonds, the bond lengths, and the distance between the gases and the surface of g-CN before and after optimization.

	CO <sub>2</sub>		NO <sub>2</sub>		HF	
	Before	After	Before	After	Before	After
Angle (°)	180°	179.42°	134.42°	129.69°	—	—
Bond lengths (Å)	1.181	1.172/1.170	1.203	1.219/1.225	0.869	0.957
$d_{\text{g-CN-gas}}$ (Å)	2.5	3.24	2.5	3.13	2.5	1.29
$E_{ads}$	-0.59 eV		-0.16 eV		-1.03 eV	
$E_{ads}$ literature	-0.226 eV [135], 0.3975 eV [134]		-0.231 eV [136]		—	

$$E_{ads} - E_{(compound-gas)} - (E_{compound} + E_{gas}), \quad (2)$$

where  $E_{(compound-gas)}$ ,  $E_{compound}$ , and  $E_{gas}$  are the total energy of gas molecules adsorbed by the surface of the compound, compound, and gas molecule, respectively. A positive adsorption energy value shows that the adsorption is energetically unfavorable, and the reaction is endothermic and hence unstable. A negative value indicates that the reaction is exothermic and hence stable and energetically favorable. The position of the nitrogen atom (N) in g-CN according to [134] shows that the adsorption energies of CO<sub>2</sub> gas on a nitrogen atom at two coordinates are more negative than those of other positions. The monolayer model was obtained by removing other layers in the unit cell of bulk.

The adsorbed CO<sub>2</sub>, NO<sub>2</sub>, and HF molecules were constructed by placing a single gas molecule parallel on the surface of compounds. The values of  $d$  for all compound-gas systems are 2.5 Å. The gas molecules CO<sub>2</sub>, NO<sub>2</sub>, and HF have bond lengths between atoms of 1.16 Å, 1.4 Å, and 0.86 Å, respectively. Top views of systems adsorbed by gas molecules are shown in Table 11. The five adsorbed models were geometrically optimized to obtain the adsorption energies and they were compared successively.

According to the optimization of the g-CN-gas system (see Table 12), the CO<sub>2</sub> and NO<sub>2</sub> molecules are moved away from the surface, while the HF molecule is brought closer to the surface. The distances between the surface of g-CN and the atoms of the molecules are 2.5 Å before optimization. After adsorption on the g-CN surface, the molecules also exhibit some deformation. The angles and bond lengths change, while the angles O-C-O and O-N-O in CO<sub>2</sub> and NO<sub>2</sub>, respectively, are decreased. The N-O and H-F bond lengths increase and the C-O bond length decreases. The distance between the surface of g-CN and the atom closest to the surface in gas molecules is noted with  $d_{\text{g-CN-gas}}$ .

The DFT calculation results show that all the adsorption energies are negative, indicating that the adsorption of the three gases on g-CN is exothermic. It can be briefly summarized that g-CN exhibits a relatively high adsorption capacity for HF (-1.03 eV) and CO<sub>2</sub> (-0.59 eV) and a low adsorption intensity for NO<sub>2</sub> (-0.166 eV). Therefore, the adsorption behavior of g-CN corresponds to efficient adsorption of reagents, which is very beneficial for gas sensor performance. The adsorption results of CO<sub>2</sub>, NO<sub>2</sub>, and HF gas molecules on g-CN showed that the  $E_{ads}$  of these gases on virgin g-CN follows the order of NO<sub>2</sub> > CO<sub>2</sub> > HF. The results suggest that the g-CN nanolayer is more stable with HF than

TABLE 13: Other potential gases detected by g-CN and their adsorption energies.

	H <sub>2</sub>	H <sub>2</sub> O	N <sub>2</sub>	CO	CH <sub>4</sub>	NO
$E_{ads}$ (eV)	-0.078	-0.513	-0.117	-0.155	-0.163 eV	-0.059 eV
Ref.	[135]				[137]	

TABLE 14: The distance between the gases and the surface of g-CN, Gr, and r-GrO before and after optimization.

	Gr		r-GrO		g-CN	
	Before	After	Before	After	Before	After
Bond lengths (Å)	0.869	0.938	0.869	0.94	0.869	0.957
$d_{\text{Gr/rGrO-HF}}$ (Å)	2.5	3.70	2.5	3.26	2.5	1.29
$E_{ads}$ (eV)	-0.04 eV		-0.74 eV		-1.03 eV	

other gases with an adsorption energy of -1.03 eV. The results revealed that the g-CN system is a suitable candidate for HF gas sensors, due to their high adsorption capacity. In addition, the results indicate that the interaction between g-CN and HF gas is significantly higher than that of other gases. Table 13 shows other gases detected by g-CN and their adsorption energies.

For Gr and r-GrO, the DFT calculation results show that the interaction of HF gas with the latter two is relatively low compared to the adsorption of HF on g-CN. The optimized structures of HF adsorbed on Gr and r-GrO are shown in Table 14. The length of the HF bond is less modified compared to its initial state of a little near ~0.94 Å. The adsorption energies of HF on Gr and r-GrO are, respectively, -0.04 eV and -0.74 eV, lower than those of HF on g-CN. This calculation shows that g-CN can be used for the detection of HF gas.

Gr-based gas sensors show commendable effect in various sensing gases. Pristine Gr shows insignificant effect in gas sensing and hence its sensitivity is enriched by either doping the Gr with suitable metal dopants such as Mg, Co, Fe, and Ni or hybridizing with other nanoparticles. Stability of the r-GrO sensors at higher temperatures is generally lower than that of g-CN based sensors. Ye et al. showed that TiO<sub>2</sub> hybridized with r-GrO senses NH<sub>3</sub> gas and the same TiO<sub>2</sub> when hybridized with g-CN shows better sensitivity for CO<sub>2</sub> even at 400°C. r-GrO based sensors are used in acidic or alkaline conditions and can sense high volatile chemicals such as chloroform. SnO<sub>2</sub>-Gr proves to be an excellent candidate for sensing humidity.

## 7. Conclusion

In this work, an overview of both Gr and g-CN low-dimensional materials was outlined in terms of elaboration and characterization with respect to their gas-sensing performances. Subsequently, theoretical calculations along with simulated gas-sensing performances of both nanomaterials were carried out to address the researcher's paradigm regarding their optimization as potential gas sensors. This sensor would exhibit high sensitivity, low detection limit, fast response, and low operating temperature. Based on our investigation, g-CN, which reveals interesting gas-sensing performances over Gr by 10-folds, may offer new opportunities for the design and manufacturing of high-performance gas sensors. This is mainly related to its semiconducting character and its porosity that provides large adsorption sites for the target gases. Besides, the conductivity and the tailorable functional groups of Gr provide a great advantage as resistive sensors. Consequently, for NO<sub>2</sub>, NH<sub>3</sub>, and organic gases such as ethanol and acetone, Gr would show high performances. The main bottlenecks are large-scale production of Gr-based sensors and sensitivity of these sensors for specific gases. The specific gas sensitivity can be improved by (1) increasing the surface area of Gr and combination with other specific nanomaterials and (2) focusing on the morphology of various GrO with specific gas adsorption [138, 139].

## Data Availability

Data collected from the literature can be consulted in the relevant articles; the authors' data are available upon request to Professor Mustapha Jouiad at mustapha.jouiad@u-picardie.fr.

## Conflicts of Interest

The authors declare that they have no conflicts of interest.

## Acknowledgments

This research was funded by a seed grant provided by MAScIR "2D-HF-Detect #240004055".

## References

- [1] A. Salas, C. Medina, J. T. Vial et al., "Ultrafast carbon nanotubes growth on recycled carbon fibers and their evaluation on interfacial shear strength in reinforced composites," *Scientific Reports*, vol. 11, no. 1, pp. 1–11, 2021.
- [2] S.-H. Chung, J. T. Kim, and D. H. Kim, "Hybrid carbon thermal interface materials for thermoelectric generator devices," *Scientific Reports*, vol. 10, no. 1, pp. 1–11, 2020.
- [3] B. Podlesny, B. Olszewska, Z. Yaari et al., "En route to single-step, two-phase purification of carbon nanotubes facilitated by high-throughput spectroscopy," *Scientific Reports*, vol. 11, no. 1, pp. 1–11, 2021.
- [4] S. Yonezawa, T. Chiba, Y. Seki, and M. Takashiri, "Origin of n type properties in single wall carbon nanotube films with anionic surfactants investigated by experimental and theoretical analyses," *Scientific Reports*, vol. 11, no. 1, pp. 1–9, 2021.
- [5] G. Deokar, J. Casanova-Cháfer, N. S. Rajput et al., "Wafer-scale few-layer graphene growth on Cu/Ni films for gas sensing applications," *Sensors and Actuators B: Chemical*, vol. 305, p. 127458, 2020.
- [6] D. D. Evanoff and G. Chumanov, "Synthesis and optical properties of silver nanoparticles and arrays," *Chem-PhysChem*, vol. 6, no. 7, pp. 1221–1231, 2005.
- [7] A. K. Bodenmann and A. H. MacDonald, "Graphene: exploring carbon flatland," *Physics Today*, vol. 60, no. 8, pp. 35–41, 2007.
- [8] Y. Si and E. T. Samulski, "Synthesis of water soluble graphene," *Nano Letters*, vol. 8, no. 6, pp. 1679–1682, 2008.
- [9] D. R. Dreyer, S. Park, C. W. Bielawski, and R. S. Ruoff, "The chemistry of graphene oxide," *Chemical Society Reviews*, vol. 39, no. 1, pp. 228–240, 2010.
- [10] G. Wang, J. Yang, J. Park et al., "Facile synthesis and characterization of graphene nanosheets," *Journal of Physical Chemistry C*, vol. 112, no. 22, pp. 8192–8195, 2008.
- [11] G. Wang, X. Shen, B. Wang, J. Yao, and J. Park, "Synthesis and characterisation of hydrophilic and organophilic graphene nanosheets," *Carbon*, vol. 47, no. 5, pp. 1359–1364, 2009.
- [12] X. Li, X. Wang, L. Zhang, S. Lee, and H. Dai, "Chemically derived, ultrasmooth graphene nanoribbon semiconductors," *Science*, vol. 319, no. 5867, pp. 1229–1232, 2008.
- [13] P. Blake, P. D. Brimicombe, R. R. Nair et al., "Graphene-based liquid crystal device," *Nano Letters*, vol. 8, no. 6, pp. 1704–1708, 2008.
- [14] J. Hu, C. Zou, Y. Su et al., "One-step synthesis of 2D C<sub>3</sub>N<sub>4</sub>-tin oxide gas sensors for enhanced acetone vapor detection," *Sensors and Actuators B: Chemical*, vol. 253, pp. 641–651, 2017.
- [15] Z. Yuan, R. Tang, Y. Zhang, and L. Yin, "Enhanced photovoltaic performance of dye-sensitized solar cells based on Co<sub>9</sub>S<sub>8</sub> nanotube array counter electrode and TiO<sub>2</sub>/g-C<sub>3</sub>N<sub>4</sub> heterostructure nanosheet photoanode," *Journal of Alloys and Compounds*, vol. 691, pp. 983–991, 2017.
- [16] S. Zhang, N. Hang, Z. Zhang, H. Yue, and W. Yang, "Preparation of g-C<sub>3</sub>N<sub>4</sub>/graphene composite for detecting NO<sub>2</sub> at room temperature," *Nanomaterials*, vol. 7, no. 1, pp. 12–11, 2017.
- [17] S. K. Ghosh, V. K. Perla, and K. Mallick, "Enhancement of dielectric and electric-field-induced polarization of bismuth fluoride nanoparticles within the layered structure of carbon nitride," *Scientific Reports*, vol. 10, no. 1, pp. 1–11, 2020.
- [18] S. Kumar, S. Karthikeyan, and A. Lee, "g-C<sub>3</sub>N<sub>4</sub>-based nanomaterials for visible light-driven photocatalysis," *Catalysts*, vol. 8, no. 2, p. 74, 2018.
- [19] S. V. Morozov, K. S. Novoselov, and A. K. Geim, "Electron transport in graphene," *Physics-Uspekhi*, vol. 51, no. 7, pp. 744–748, 2008.
- [20] A. N. Sruti and K. Jagannadham, "Electrical conductivity of graphene composites with in and In-Ga alloy," *Journal of Electronic Materials*, vol. 39, no. 8, pp. 1268–1276, 2010.
- [21] F. Schedin, A. K. Geim, S. V. Morozov et al., "Detection of individual gas molecules adsorbed on graphene," *Nature Materials*, vol. 6, no. 9, pp. 652–655, 2007.
- [22] G. Lu, L. E. Ocola, and J. Chen, "Reduced graphene oxide for room-temperature gas sensors," *Nanotechnology*, vol. 20, no. 44, p. 445502, 2009.
- [23] S. Li, Z. Wang, X. Wang et al., "Orientation controlled preparation of nanoporous carbon nitride fibers and related

- composite for gas sensing under ambient conditions,” *Nano Research*, vol. 10, no. 5, pp. 1710–1719, 2017.
- [24] Q. Ma, B. Kutlik, N. Kari, S. Abliz, and A. Yimit, “Study on surface sensitization of g-C<sub>3</sub>N<sub>4</sub> by functionalized different aggregation behavior porphyrin and its optical properties,” *Materials Science in Semiconductor Processing*, vol. 121, p. 105316, 2021.
- [25] S. Absalan, S. Nasresfahani, and M. H. Sheikhi, “High-performance carbon monoxide gas sensor based on palladium/tin oxide/porous graphitic carbon nitride nanocomposite,” *Journal of Alloys and Compounds*, vol. 795, pp. 79–90, 2019.
- [26] G. Deokar, J. Avila, I. Razado-Colambo et al., “Towards high quality CVD graphene growth and transfer,” *Carbon*, vol. 89, pp. 82–92, 2015.
- [27] H. Asgar, K. M. Deen, U. Riaz, Z. U. Rahman, U. H. Shah, and W. Haider, “Synthesis of graphene via ultra-sonic exfoliation of graphite oxide and its electrochemical characterization,” *Materials Chemistry and Physics*, vol. 206, pp. 7–11, 2018.
- [28] K. S. Novoselov, A. Mishchenko, A. Carvalho, and A. H. Castro Neto, “2D materials and van der Waals heterostructures,” *Science*, vol. 353, no. 6298, p. 353, 2016.
- [29] M. Yi and Z. Shen, “A review on mechanical exfoliation for the scalable production of graphene,” *Journal of Materials Chemistry*, vol. 3, no. 22, pp. 11700–11715, 2015.
- [30] G. Deokar, A. Genovese, and P. M. F. J. Costa, “Fast, wafer-scale growth of a nanometer-thick graphite film on Ni foil and its structural analysis,” *Nanotechnology*, vol. 31, no. 48, p. 485605, 2020.
- [31] G. Deokar, J.-L. Codron, C. Boyaval, X. Wallart, and D. Vignaud, “CVD graphene growth on Ni films and transfer,” in *Proceedings of the 4th Graphene Conference, Graphene*, Toulouse, France, July 2014.
- [32] D. Mouloua, A. Kotbi, G. Deokar et al., “Recent progress in the synthesis of MoS<sub>2</sub> thin films for sensing, photovoltaic and plasmonic applications: a review,” *Materials*, vol. 14, no. 12, p. 3283, 2021.
- [33] Q. Yu, J. Lian, S. Siriponglert, H. Li, Y. P. Chen, and S.-S. Pei, “Graphene segregated on Ni surfaces and transferred to insulators,” *Applied Physics Letters*, vol. 93, no. 11, pp. 113103–113104, 2008.
- [34] G. Deokar, A. Genovese, S. G. Surya, C. Long, K. N. Salama, and P. M. F. J. Costa, “Semi-transparent graphite films growth on Ni and their double-sided polymer-free transfer,” *Scientific Reports*, vol. 10, no. 1, pp. 1–15, 2020.
- [35] X. Li, W. Cai, J. An et al., “Large-area synthesis of high-quality and uniform graphene films on copper foils,” *Science*, vol. 324, no. 5932, pp. 1312–1314, 2009.
- [36] A. K. Geim, “GRAPHENE: STATUS and prospects A. K. Geim manchester centre for mesoscience and nanotechnology,” *Prospects*, vol. 324, pp. 1–8, 2009.
- [37] K. V. Emtsev, A. Bostwick, K. Horn et al., “Towards wafer-size graphene layers by atmospheric pressure graphitization of silicon carbide,” *Nature Materials*, vol. 8, no. 3, pp. 203–207, 2009.
- [38] K. S. Kim, Y. Zhao, H. Jang et al., “Large-scale pattern growth of graphene films for stretchable transparent electrodes,” *Nature*, vol. 457, no. 7230, pp. 706–710, 2009.
- [39] S. Bae, H. Kim, Y. Lee et al., “Roll-to-roll production of 30-inch graphene films for transparent electrodes,” *Nature Nanotechnology*, vol. 5, no. 8, pp. 574–578, 2010.
- [40] X. Li, C. W. Magnuson, A. Venugopal et al., “Graphene films with large domain size by a two-step chemical vapor deposition process,” *Nano Letters*, vol. 10, no. 11, pp. 4328–4334, 2010.
- [41] K. S. Novoselov, A. K. Geim, S. V. Morozov et al., “Two-dimensional gas of massless Dirac fermions in graphene,” *Nature*, vol. 438, no. 7065, pp. 197–200, 2005.
- [42] R. Kaindl, G. Jakopic, R. Resel et al., “Synthesis of graphene-layer nanosheet coatings by PECVD,” *Materials Today Proceedings*, vol. 2, no. 8, pp. 4247–4255, 2015.
- [43] N. Li, Z. Zhen, R. Zhang, Z. Xu, Z. Zheng, and L. He, “Nucleation and growth dynamics of graphene grown by radio frequency plasma-enhanced chemical vapor deposition,” *Scientific Reports*, vol. 11, no. 1, pp. 1–10, 2021.
- [44] N. Woehrl, O. Ochedowski, S. Gottlieb, K. Shibasaki, and S. Schulz, “Plasma-enhanced chemical vapor deposition of graphene on copper substrates,” *AIP Advances*, vol. 4, no. 4, p. 47128, 2014.
- [45] C. Yang, H. Bi, D. Wan, F. Huang, X. Xie, and M. Jiang, “Direct PECVD growth of vertically erected graphene walls on dielectric substrates as excellent multifunctional electrodes,” *Journal of Materials Chemistry*, vol. 1, no. 3, pp. 770–775, 2013.
- [46] S. Hussain, E. Kovacevic, J. Berndt et al., “Low-temperature low-power PECVD synthesis of vertically aligned graphene,” *Nanotechnology*, vol. 31, no. 39, p. 395604, 2020.
- [47] S. Chugh, R. Mehta, N. Lu, F. D. Dios, M. J. Kim, and Z. Chen, “Comparison of graphene growth on arbitrary non-catalytic substrates using low-temperature PECVD,” *Carbon*, vol. 93, pp. 393–399, 2015.
- [48] B. Gürünlü, Ç. Taşdelen Yücedağ, and M. R. Bayramoğlu, “Green synthesis of graphene from graphite in molten salt medium,” *Journal of Nanomaterials*, vol. 2020, Article ID 7029601, 12 pages, 2020.
- [49] G. Varshney, S. R. Kanel, D. M. Kempisty et al., “Nanoscale TiO<sub>2</sub> films and their application in remediation of organic pollutants,” *Coordination Chemistry Reviews*, vol. 306, pp. 43–64, 2016.
- [50] B. Priyadarshini, M. Rama, and U. Vijayalakshmi, “Bioactive coating as a surface modification technique for biocompatible metallic implants: a review,” *Journal of Asian Ceramic Societies*, vol. 7, no. 4, pp. 397–406, 2019.
- [51] L. Ye and S. Chen, “Fabrication and high visible-light-driven photocurrent response of g-C<sub>3</sub>N<sub>4</sub> film: the role of thiourea,” *Applied Surface Science*, vol. 389, pp. 1076–1083, 2016.
- [52] R. Tejasvi and S. Basu, “Formation of C<sub>3</sub>N<sub>4</sub> thin films through the stoichiometric transfer of the bulk synthesized gC<sub>3</sub>N<sub>4</sub> using RFM sputtering,” *Vacuum*, vol. 171, p. 108937, 2020.
- [53] Y. Shi, L. He, F. Guang, L. Li, Z. Xin, and R. Liu, “A review: preparation, performance, and applications of silicon oxynitride film,” *Micromachines*, vol. 10, no. 8, pp. 552–623, 2019.
- [54] N. A. Mohamed, J. Safaei, A. F. Ismail et al., “The influences of post-annealing temperatures on fabrication graphitic carbon nitride, (g-C<sub>3</sub>N<sub>4</sub>) thin film,” *Applied Surface Science*, vol. 489, pp. 92–100, 2019.
- [55] X. Sun, X. An, S. Zhang et al., “Physical vapor deposition (PVD): a method to fabricate modified g-C<sub>3</sub>N<sub>4</sub> sheets,” *New Journal of Chemistry*, vol. 43, no. 17, pp. 6683–6687, 2019.
- [56] J. Huang, J. Hu, Y. Shi et al., “Evaluation of self-cleaning and photocatalytic properties of modified g-C<sub>3</sub>N<sub>4</sub> based PVDF membranes driven by visible light,” *Journal of Colloid and Interface Science*, vol. 541, pp. 356–366, 2019.
- [57] G. Zhang, J. Zhang, M. Zhang, and X. Wang, “Polycondensation of thiourea into carbon nitride semiconductors as

- visible light photocatalysts," *Journal of Materials Chemistry*, vol. 22, no. 16, pp. 8083–8091, 2012.
- [58] Y. Zhang, J. Liu, X. Chu, S. Liang, and L. Kong, "Preparation of g-C<sub>3</sub>N<sub>4</sub>-SnO<sub>2</sub> composites for application as acetic acid sensor," *Journal of Alloys and Compounds*, vol. 832, p. 153355, 2020.
- [59] D. Wang, W. Gu, Y. Zhang et al., "Novel C-rich carbon nitride for room temperature NO<sub>2</sub> gas sensors," *RSC Advances*, vol. 4, no. 35, pp. 18003–18006, 2014.
- [60] X. Li, J. Xiong, X. Gao et al., "Recent advances in 3D g-C<sub>3</sub>N<sub>4</sub> composite photocatalysts for photocatalytic water splitting, degradation of pollutants and CO<sub>2</sub> reduction," *Journal of Alloys and Compounds*, vol. 802, pp. 196–209, 2019.
- [61] M. Ismael, Y. Wu, D. H. Taffa, P. Bottke, and M. Wark, "Graphitic carbon nitride synthesized by simple pyrolysis: role of precursor in photocatalytic hydrogen production," *New Journal of Chemistry*, vol. 43, no. 18, pp. 6909–6920, 2019.
- [62] W. Zhang, Z. Zhao, F. Dong, and Y. Zhang, "Solvent-assisted synthesis of porous g-C<sub>3</sub>N<sub>4</sub> with efficient visible-light photocatalytic performance for NO removal," *Chinese Journal of Catalysis*, vol. 38, no. 2, pp. 372–378, 2017.
- [63] S. Yao, S. Xue, S. Peng et al., "Synthesis of graphitic carbon nitride via direct polymerization using different precursors and its application in lithium-sulfur batteries," *Applied Physics A*, vol. 124, no. 11, pp. 1–10, 2018.
- [64] J. Tian, Z. Chen, J. Jing, C. Feng, M. Sun, and W. Li, "Enhanced photocatalytic performance of the MoS<sub>2</sub>/g-C<sub>3</sub>N<sub>4</sub> heterojunction composite prepared by vacuum freeze drying method," *Journal of Photochemistry and Photobiology A: Chemistry*, vol. 390, p. 112260, 2020.
- [65] W. Iqbal, B. Yang, X. Zhao et al., "Facile one-pot synthesis of mesoporous g-C<sub>3</sub>N<sub>4</sub> nanosheets with simultaneous iodine doping and N-vacancies for efficient visible-light-driven H<sub>2</sub> evolution performance," *Catalysis Science and Technology*, vol. 10, no. 2, pp. 549–559, 2020.
- [66] R. M. Yadav, R. Kumar, A. Aliyan et al., "Facile synthesis of highly fluorescent free-standing films comprising graphitic carbon nitride (g-C<sub>3</sub>N<sub>4</sub>) nanolayers," *New Journal of Chemistry*, vol. 44, no. 6, pp. 2644–2651, 2020.
- [67] Y. Wang, F. Wang, Y. Zuo, X. Zhang, and L.-F. Cui, "Simple synthesis of ordered cubic mesoporous graphitic carbon nitride by chemical vapor deposition method using melamine," *Materials Letters*, vol. 136, pp. 271–273, 2014.
- [68] Z. Wei, Z. Zhi-Hong, G. Huai-Xi, X. Yi, and F. Xiang-Jun, "Corrosion resistance properties and preparation of  $\alpha$ -C<sub>3</sub>N<sub>4</sub> thin films," *Wuhan University Journal of Natural Sciences*, vol. 4, no. 2, pp. 171–174, 1999.
- [69] Z. Xiong and L. Cao, "Nanostructure and optical property tuning between the graphitic-like CN<sub>x</sub> and fullerene-like  $\beta$ -C<sub>3</sub>N<sub>4</sub> via Fe doping and substrate temperature," *Journal of Alloys and Compounds*, vol. 775, pp. 100–108, 2019.
- [70] L. Cai, X. Wei, H. Feng et al., "Antimicrobial mechanisms of g-C<sub>3</sub>N<sub>4</sub> nanosheets against the oomycetes *Phytophthora capsici*: disrupting metabolism and membrane structures and inhibiting vegetative and reproductive growth," *Journal of Hazardous Materials*, vol. 417, p. 126121, 2021.
- [71] Y. Bu, Z. Chen, J. Yu, and W. Li, "A novel application of g-C<sub>3</sub>N<sub>4</sub> thin film in photoelectrochemical anticorrosion," *Electrochimica Acta*, vol. 88, pp. 294–300, 2013.
- [72] V. Guigoz, L. Balan, A. Aboulaich, R. Schneider, and T. Gries, "Heterostructured thin LaFeO<sub>3</sub>/g-C<sub>3</sub>N<sub>4</sub> films for efficient photoelectrochemical hydrogen evolution," *International Journal of Hydrogen Energy*, vol. 45, no. 35, pp. 17468–17479, 2020.
- [73] W. Zhang, L. Zhou, and H. Deng, "Ag modified g-C<sub>3</sub>N<sub>4</sub> composites with enhanced visible-light photocatalytic activity for diclofenac degradation," *Journal of Molecular Catalysis A: Chemical*, vol. 423, pp. 270–276, 2016.
- [74] H. Miao, G. Zhang, X. Hu et al., "A novel strategy to prepare 2D g-C<sub>3</sub>N<sub>4</sub> nanosheets and their photoelectrochemical properties," *Journal of Alloys and Compounds*, vol. 690, pp. 669–676, 2017.
- [75] G. Yang, T. Chen, B. Feng et al., "Improved corrosion resistance and biocompatibility of biodegradable magnesium alloy by coating graphite carbon nitride (g-C<sub>3</sub>N<sub>4</sub>)," *Journal of Alloys and Compounds*, vol. 770, pp. 823–830, 2019.
- [76] J. Jiang, L. Ou-Yang, L. Zhu et al., "Dependence of electronic structure of g-C<sub>3</sub>N<sub>4</sub> on the layer number of its nanosheets: a study by Raman spectroscopy coupled with first-principles calculations," *Carbon*, vol. 80, pp. 213–221, 2014.
- [77] J. Kavil, S. Pilathottathil, M. S. Thayyil, and P. Periyat, "Development of 2D nano heterostructures based on g-C<sub>3</sub>N<sub>4</sub> and flower shaped MoS<sub>2</sub> as electrode in symmetric supercapacitor device," *Nano-Structures & Nano-Objects*, vol. 18, p. 100317, 2019.
- [78] N. Duraisamy and K. Kandiah, "Binder-free heterostructure (g-C<sub>3</sub>N<sub>4</sub>/PPy) based thin film on semi-flexible nickel foam via hybrid spray technique for energy storage application," *Progress in Natural Science: Materials International*, vol. 30, no. 3, pp. 298–307, 2020.
- [79] Q. Gu, Y. Liao, L. Yin, J. Long, X. Wang, and C. Xue, "Template-free synthesis of porous graphitic carbon nitride microspheres for enhanced photocatalytic hydrogen generation with high stability," *Applied Catalysis B: Environmental*, vol. 165, pp. 503–510, 2015.
- [80] S. Panimalar, R. Uthrakumar, E. T. Selvi et al., "Studies of MnO<sub>2</sub>/g-C<sub>3</sub>N<sub>4</sub> heterostructure efficient of visible light photocatalyst for pollutants degradation by sol-gel technique," *Surfaces and Interfaces*, vol. 20, p. 100512, 2020.
- [81] A. Kotbi, B. Hartiti, S. Fadili, A. Ridah, and P. Thevenin, "Experimental and theoretical studies of CuInS<sub>2</sub> thin films for photovoltaic applications," *Journal of Materials Science: Materials in Electronics*, vol. 30, no. 24, pp. 21096–21105, 2019.
- [82] G. Deokar, P. Vancsó, R. Arenal et al., "MoS<sub>2</sub>-carbon nanotube hybrid material growth and gas sensing," *Advanced Materials Interfaces*, vol. 4, no. 24, pp. 1700801–1700810, 2017.
- [83] N. Joshi, T. Hayasaka, Y. Liu, H. Liu, O. N. Oliveira, and L. Lin, "A review on chemiresistive room temperature gas sensors based on metal oxide nanostructures, graphene and 2D transition metal dichalcogenides," *Microchimica Acta*, vol. 185, no. 4, 2018.
- [84] Y.-H. Zhang, Y.-B. Chen, K.-G. Zhou et al., "Improving gas sensing properties of graphene by introducing dopants and defects: a first-principles study," *Nanotechnology*, vol. 20, no. 18, p. 185504, 2009.
- [85] L. Shao, G. Chen, H. Ye et al., "Sulfur dioxide adsorbed on graphene and heteroatom-doped graphene: a first-principles study," *The European Physical Journal B*, vol. 86, no. 2, pp. 2–6, 2013.
- [86] Y.-H. Zhang, L.-F. Han, Y.-H. Xiao, D.-Z. Jia, Z.-H. Guo, and F. Li, "Understanding dopant and defect effect on H<sub>2</sub>S sensing performances of graphene: a first-principles study," *Computational Materials Science*, vol. 69, pp. 222–228, 2013.

- [87] C. Ma, X. Shao, and D. Cao, "Nitrogen-doped graphene as an excellent candidate for selective gas sensing," *Science China Chemistry*, vol. 57, no. 6, pp. 911–917, 2014.
- [88] Z. Rajesh Gao, A. T. Charlie Johnson, N. Puri, A. Mulchandani, and D. K. Aswal, "Scalable chemical vapor deposited graphene field-effect transistors for bio/chemical assay," *Applied Physics Reviews*, vol. 8, no. 1, p. 011311, 2021.
- [89] G. Ko, H.-Y. Kim, J. Ahn, Y.-M. Park, K.-Y. Lee, and J. Kim, "Graphene-based nitrogen dioxide gas sensors," *Current Applied Physics*, vol. 10, no. 4, pp. 1002–1004, 2010.
- [90] G. Chen, T. M. Paronyan, and A. R. Harutyunyan, "Sub-ppt gas detection with pristine graphene," *Applied Physics Letters*, vol. 101, no. 5, p. 053119, 2012.
- [91] W. Kang and S. Park, "H<sub>2</sub>S gas sensing properties of CuO nanotubes," *Applied Science and Convergence Technology*, vol. 23, no. 6, pp. 392–397, 2014.
- [92] S. Prezioso, F. Perrozzi, L. Giancaterini et al., "Graphene oxide as a practical solution to high sensitivity gas sensing," *Journal of Physical Chemistry C*, vol. 117, no. 20, pp. 10683–10690, 2013.
- [93] J. Wang, B. Singh, J.-H. Park et al., "Dielectrophoresis of graphene oxide nanostructures for hydrogen gas sensor at room temperature," *Sensors and Actuators B: Chemical*, vol. 194, pp. 296–302, 2014.
- [94] S. Drewniak, T. Pustelny, M. Setkiewicz et al., "Investigations of SAW structures with oxide graphene layer to detection of selected gases," *Acta Physica Polonica A*, vol. 124, no. 3, pp. 402–405, 2013.
- [95] T. Pustelny, S. Drewniak, M. Setkiewicz et al., "The sensitivity of sensor structures with oxide graphene exposed to selected gaseous atmospheres," *Bulletin of the Polish Academy of Sciences, Technical Sciences*, vol. 61, no. 3, pp. 705–710, 2013.
- [96] S. Some, Y. Xu, Y. Kim et al., "Highly sensitive and selective gas sensor using hydrophilic and hydrophobic graphenes," *Scientific Reports*, vol. 3, no. 1, pp. 19–22, 2013.
- [97] J. Hassinen, J. Kauppila, J. Leiro et al., "Low-cost reduced graphene oxide-based conductometric nitrogen dioxide-sensitive sensor on paper," *Analytical and Bioanalytical Chemistry*, vol. 405, no. 11, pp. 3611–3617, 2013.
- [98] Y. Pak, S.-M. Kim, H. Jeong et al., "Palladium-decorated hydrogen-gas sensors using periodically aligned graphene nanoribbons," *ACS Applied Materials & Interfaces*, vol. 6, no. 15, pp. 13293–13298, 2014.
- [99] M. G. Chung, D.-H. Kim, D. K. Seo et al., "Flexible hydrogen sensors using graphene with palladium nanoparticle decoration," *Sensors and Actuators B: Chemical*, vol. 169, pp. 387–392, 2012.
- [100] A. Kaniyoor, R. Imran Jafri, T. Arockiadoss, and S. Ramaprabhu, "Nanostructured Pt decorated graphene and multi walled carbon nanotube based room temperature hydrogen gas sensor," *Nanoscale*, vol. 1, no. 3, pp. 382–386, 2009.
- [101] W. Li, X. Geng, Y. Guo et al., "Reduced graphene oxide electrically contacted graphene sensor for highly sensitive nitric oxide detection," *ACS Nano*, vol. 5, no. 9, pp. 6955–6961, 2011.
- [102] A. Gutiérrez, B. Hsia, A. Sussman et al., "Graphene decoration with metal nanoparticles: towards easy integration for sensing applications," *Nanoscale*, vol. 4, no. 2, pp. 438–440, 2012.
- [103] P. Karthik, P. Gowthaman, M. Venkatachalam, and M. Saroja, "Design and fabrication of g-C<sub>3</sub>N<sub>4</sub> nanosheets decorated TiO<sub>2</sub> hybrid sensor films for improved performance towards CO<sub>2</sub> gas," *Inorganic Chemistry Communications*, vol. 119, p. 108060, 2020.
- [104] L. Zhu, Y. Jia, G. Gai, X. Ji, J. Luo, and Y. Yao, "Ambipolarity of large-area Pt-functionalized graphene observed in H<sub>2</sub> sensing," *Sensors and Actuators B: Chemical*, vol. 190, pp. 134–140, 2014.
- [105] J. Yu, M. Shafiei, J. Ou, K. Shin, and W. Wlodarski, "A study of hydrogen gas sensing performance of Pt/Graphene/GaN devices," *2011 IEEE SENSORS Proceedings*, pp. 1017–1020, 2011.
- [106] K. Anand, O. Singh, M. P. Singh, J. Kaur, and R. C. Singh, "Hydrogen sensor based on graphene/ZnO nanocomposite," *Sensors and Actuators B: Chemical*, vol. 195, pp. 409–415, 2014.
- [107] A. Esfandiari, A. Irajizad, O. Akhavan, S. Ghasemi, and M. R. Gholami, "Pd-WO<sub>3</sub>/reduced graphene oxide hierarchical nanostructures as efficient hydrogen gas sensors," *International Journal of Hydrogen Energy*, vol. 39, no. 15, pp. 8169–8179, 2014.
- [108] M. Shafiei, R. Arsat, J. Yu, and W. Wlodarski, "Pt/graphene nano-sheet based hydrogen gas sensor," *IEEE*, vol. 2009, pp. 295–298, 2009.
- [109] X. Liu, J. Cui, J. Sun, and X. Zhang, "3D graphene aerogel-supported SnO<sub>2</sub> nanoparticles for efficient detection of NO<sub>2</sub>," *RSC Advances*, vol. 4, no. 43, pp. 22601–22605, 2014.
- [110] S. Srivastava, K. Jain, V. N. Singh et al., "Faster response of NO<sub>2</sub> sensing in graphene-WO<sub>3</sub> nanocomposites," *Nanotechnology*, vol. 23, no. 20, p. 205501, 2012.
- [111] H. Y. Jeong, D.-S. Lee, H. K. Choi et al., "Flexible room-temperature NO<sub>2</sub> gas sensors based on carbon nanotubes/reduced graphene hybrid films," *Applied Physics Letters*, vol. 96, no. 21, pp. 213105–213197, 2010.
- [112] L. T. Hoa, H. N. Tien, V. H. Luan, J. S. Chung, and S. H. Hur, "Fabrication of a novel 2D-graphene/2D-NiO nanosheet-based hybrid nanostructure and its use in highly sensitive NO<sub>2</sub> sensors," *Sensors and Actuators B: Chemical*, vol. 185, pp. 701–705, 2013.
- [113] S. Liu, B. Yu, H. Zhang, T. Fei, and T. Zhang, "Enhancing NO<sub>2</sub> gas sensing performances at room temperature based on reduced graphene oxide-ZnO nanoparticles hybrids," *Sensors and Actuators B: Chemical*, vol. 202, pp. 272–278, 2014.
- [114] N. Chen, X. Li, X. Wang et al., "Enhanced room temperature sensing of Co<sub>3</sub>O<sub>4</sub>-intercalated reduced graphene oxide based gas sensors," *Sensors and Actuators B: Chemical*, vol. 188, pp. 902–908, 2013.
- [115] H. Zhang, J. Feng, T. Fei, S. Liu, and T. Zhang, "SnO<sub>2</sub> nanoparticles-reduced graphene oxide nanocomposites for NO<sub>2</sub> sensing at low operating temperature," *Sensors and Actuators B: Chemical*, vol. 190, pp. 472–478, 2014.
- [116] X. An, J. C. Yu, Y. Wang, Y. Hu, X. Yu, and G. Zhang, "WO<sub>3</sub> nanorods/graphene nanocomposites for high-efficiency visible-light-driven photocatalysis and NO<sub>2</sub> gas sensing," *Journal of Materials Chemistry*, vol. 22, no. 17, pp. 8525–8531, 2012.
- [117] K. R. Nemade and S. A. Waghuley, "Role of defects concentration on optical and carbon dioxide gas sensing properties of Sb<sub>2</sub>O<sub>3</sub>/graphene composites," *Optical Materials*, vol. 36, no. 3, pp. 712–716, 2014.
- [118] K. R. Nemade and S. A. Waghuley, "Highly responsive carbon dioxide sensing by graphene/Al<sub>2</sub>O<sub>3</sub> quantum dots composites at low operable temperature," *Indian Journal of Physics*, vol. 88, no. 6, pp. 577–583, 2014.

- [119] K. R. Nemade and S. A. Waghuley, "LPG sensing application of graphene/Bi<sub>2</sub>O<sub>3</sub> quantum dots composites," *Solid State Sciences*, vol. 22, pp. 27–32, 2013.
- [120] X. Tang, M. Debliquy, D. Lahem, Y. Yan, and J.-P. Raskin, "A review on functionalized graphene sensors for detection of ammonia," *Sensors*, vol. 21, no. 4, pp. 1443–1528, 2021.
- [121] B. Electrochemical and A. Overview: An Overview.
- [122] X. Huang, N. Hu, R. Gao et al., "Reduced graphene oxide-polyaniline hybrid: preparation, characterization and its applications for ammonia gas sensing," *Journal of Materials Chemistry*, vol. 22, no. 42, pp. 22488–22495, 2012.
- [123] D. Sahni, A. Jea, J. A. Mata et al., "Biocompatibility of pristine graphene for neuronal interface," *Journal of Neurosurgery: Pediatrics*, vol. 11, no. 5, pp. 575–583, 2013.
- [124] A. I. Cooper and M. J. Bojdys, "Carbon nitride vs. graphene - now in 2D!" *Materials Today*, vol. 17, no. 10, pp. 468–469, 2014.
- [125] X. Chu, J. Liu, S. Liang, L. Bai, Y. Dong, and M. Epifani, "Facile preparation of g-C<sub>3</sub>N<sub>4</sub>-WO<sub>3</sub> composite gas sensing materials with enhanced gas sensing selectivity to acetone," *Journal of Sensors*, vol. 2019, Article ID 6074046, 8 pages, 2019.
- [126] R. Zhang, Y. Wang, Z. Zhang, and J. Cao, "Highly sensitive acetone gas sensor based on g-C<sub>3</sub>N<sub>4</sub> decorated MgFe<sub>2</sub>O<sub>4</sub> porous microspheres composites," *Sensors*, vol. 18, no. 7, p. 2211, 2018.
- [127] N. T. Hang, S. Zhang, and W. Yang, "Efficient exfoliation of g-C<sub>3</sub>N<sub>4</sub> and NO<sub>2</sub> sensing behavior of graphene/g-C<sub>3</sub>N<sub>4</sub> nanocomposite," *Sensors and Actuators B: Chemical*, vol. 248, pp. 940–948, 2017.
- [128] H. Wang, J. Bai, M. Dai et al., "Visible light activated excellent NO<sub>2</sub> sensing based on 2D/2D ZnO/g-C<sub>3</sub>N<sub>4</sub> heterojunction composites," *Sensors and Actuators B: Chemical*, vol. 304, p. 127287, 2020.
- [129] S. Yang, C. Jiang, and S.-h. Wei, "Gas sensing in 2D materials," *Applied Physics Reviews*, vol. 4, no. 2, p. 021304, 2017.
- [130] J. P. Perdew, K. Burke, and M. Ernzerhof, "Generalized gradient approximation made simple," *Physical Review Letters*, vol. 77, no. 18, pp. 3865–3868, 1996.
- [131] P. Giannozzi, S. Baroni, N. Bonini et al., "Quantum espresso: a modular and open-source software project for quantum simulations of materials," *Journal of Physics: Condensed Matter*, vol. 21, no. 39, p. 395502, 2009.
- [132] H. W. Zuo, C. H. Lu, Y. R. Ren, Y. Li, Y. F. Zhang, and W. K. Chen, "Pt<sub>4</sub> clusters supported on monolayer graphitic carbon nitride sheets for oxygen adsorption: a first-principles study," *Wu Li Hua Xue Xue Bao/Acta Physico - Chimica Sinica*, vol. 32, pp. 1183–1190, 2016.
- [133] H.-Z. Wu, L.-M. Liu, and S.-J. Zhao, "The effect of water on the structural, electronic and photocatalytic properties of graphitic carbon nitride," *Physical Chemistry Chemical Physics*, vol. 16, no. 7, pp. 3299–3304, 2014.
- [134] B. Zhu, L. Zhang, D. Xu, B. Cheng, and J. Yu, "Adsorption investigation of CO<sub>2</sub> on g-C<sub>3</sub>N<sub>4</sub> surface by DFT calculation," *Journal of CO<sub>2</sub> Utilization*, vol. 21, pp. 327–335, 2017.
- [135] Y. Ji, H. Dong, H. Lin, L. Zhang, T. Hou, and Y. Li, "Heptazine-based graphitic carbon nitride as an effective hydrogen purification membrane," *RSC Advances*, vol. 6, no. 57, pp. 52377–52383, 2016.
- [136] H. Basharnavaz, A. Habibi-Yangjeh, and S. H. Kamali, "A first-principle investigation of NO<sub>2</sub> adsorption behavior on Co, Rh, and Ir-embedded graphitic carbon nitride: looking for highly sensitive gas sensor," *Physics Letters A*, vol. 384, no. 2, p. 126057, 2020.
- [137] K. Bai, Z. Cui, E. Li et al., "Adsorption of gas molecules on group III atoms adsorbed g-C<sub>3</sub>N<sub>4</sub>: a first-principles study," *Vacuum*, vol. 175, p. 109293, 2020.
- [138] I. T. Jolliffe and J. Cadima, "Principal component analysis: a review and recent developments," *Philosophical Transactions of the Royal Society A: Mathematical, Physical & Engineering Sciences*, vol. 374, no. 2065, p. 20150202, 2016.
- [139] R. Haney, N. Siddiqui, J. Andress, J. Fergus, R. Overfelt, and B. Prorok, "Principal component analysis (PCA) application to FTIR spectroscopy data of CO/CO<sub>2</sub> contaminants of air," *41st International Conference on Environmental Systems*, vol. 2011, pp. 1–12, 2011.